

Banner appropriate to article type will appear here in typeset article

Nonlinear evolution of vortical disturbances entrained in the entrance region of a channel

Kaixin Zhu¹† and Pierre Ricco¹

¹School of Mechanical, Aerospace and Civil Engineering, The University of Sheffield, Sheffield, S1 3JD, UK

(Received xx; revised xx; accepted xx)

Accepted for publication in *J. Fluid Mech.*

The nonlinear evolution of free-stream vortical disturbances entrained in the entrance region of a channel is investigated using asymptotic and numerical methods, building on the linear framework developed by Ricco & Alvarenga (*J. Fluid Mech.*, vol. 927, 2021). The focus is on low-frequency disturbances that induce streamwise-elongated structures at Reynolds numbers for which the entrance flow is locally stable according to classical linear stability theory. The perturbation flow along the channel entrance is generated by free-stream vortical disturbances located at the channel inlet. These disturbances are symmetric or antisymmetric with respect to the centreplane and their amplitude is sufficiently intense to provoke nonlinear interactions within the channel. The formation and evolution of the perturbation flow are described by the nonlinear unsteady boundary-region equations. Combined with physically realistic initial conditions, the resulting initial-boundary-value problems are solved numerically using a streamwise integration method. A parametric study is conducted to elucidate how the nonlinear channel flow is influenced by the Reynolds number and the inlet-disturbance properties, i.e. the amplitude and the streamwise, wall-normal, and spanwise wavelengths. Nonlinearity is found to stabilise the intense algebraic growth and to drive the formation of elongated channel-entrance structures that span the entire cross-section. These structures, characterised by low- and high-speed regions and streamwise vortices, meander along the streamwise direction and persist even when the base flow is fully developed. They exhibit a half-turn rotational symmetry with respect to the vortex centres. These properties emerge downstream regardless of the symmetry of the initial perturbation flow, provided nonlinear interactions are sufficiently intense. The occurrence of travelling waves is detected sufficiently downstream, and their similarity to those found in the fully developed region by other researchers is discussed. Our results show good agreement with theoretical predictions, numerical results and experimental measurements for both the mean flow and the perturbation flow.

Key words:

† Email address for correspondence: k.zhu1@imperial.ac.uk

1. Introduction

Laminar–turbulent transition in confined shear flows remains a central problem in fluid mechanics because of its fundamental significance and its broad engineering applications. In channel flows, the pressure gradient required to sustain turbulence is substantially larger than that required for laminar motion, making accurate prediction of transition essential for design and operation.

In several canonical confined flows, classical linear stability theory has failed to account for the observed transition. Plane Couette flow and Hagen–Poiseuille flow are predicted to be linearly stable at all Reynolds numbers (Drazin & Reid 2004), yet experiments show transition at moderate Reynolds numbers. Even in plane Poiseuille flow, for which linear theory predicts a critical Reynolds number $Re_c = 5772.22$ (Orszag 1971) (where Re_c is based on the half-channel height and the centreplane velocity), transition is observed experimentally at substantially lower Reynolds numbers. These discrepancies have motivated extensive research on subcritical transition and nonlinear disturbance growth in fully developed channel flow.

In contrast, considerably less attention has been given to the entrance region of a channel, where the velocity profile and pressure gradient vary in the streamwise direction. This spatial development fundamentally alters both the base flow and the mechanisms by which disturbances evolve. Since the laminar entrance length grows linearly with the bulk Reynolds number Re_b (based on half channel height) for $Re_b > 100$ (Durst *et al.* 2005), it can extend over a very long downstream distance at high Reynolds numbers. Channel-entrance flow has indeed been experimentally maintained laminar up to $Re_b > 5000$ in a channel of length 821.9 half-heights (Nishioka *et al.* 1975). It is however still unclear how vortical disturbances amplify nonlinearly and evolve along this long spatially developing region. In this paper, we thus aim to investigate the flow in the entrance region of a channel, with particular focus on how entrained vortical disturbances grow nonlinearly and evolve downstream.

We review the relevant studies on stability and transition in fully developed channel flows in §1.1 and in channel-entrance flows in §1.2. We discuss the boundary-region framework in §1.3 and outline the objectives of the present study in §1.4.

1.1. Fully developed channel flow

The linear stability analysis of fully developed channel flow leads to the Orr–Sommerfeld and Squire equations with homogeneous boundary conditions at the channel walls. The Orr–Sommerfeld equation was initially solved by asymptotic methods (Heisenberg 1924; Lin 1946; Shen 1954; Stuart 1963) and later by numerical methods (Thomas 1953; Grosch & Salwen 1968; Orszag 1971). The critical Reynolds numbers Re_c obtained in these studies all lie between 5000 and 6000. Experimental studies of laminar–turbulent transition in fully developed channel flow date back to Davies & White (1928), who conducted a series of measurements in a rectangular water channel with a width–height aspect ratio ranging from 37 to 165. The transitional Reynolds number was found to be $Re_b = 1440$ for channels with aspect ratios larger than 70. Subsequent investigations by Patel & Head (1969), Kao & Park (1970) and Carlson *et al.* (1982) observed transition for $Re_b < 3000$. The deviation of experimental observations from theoretical predictions arises from the subcritical nature of transition in channel flow. The experimental measurements performed by Nishioka *et al.* (1975) and Nishioka *et al.* (1981) demonstrated the downstream development of disturbances triggered by a vibrating ribbon in the fully developed region. The nonlinear subcritical instability occurred when the disturbance amplitude exceeded a certain threshold, in agreement with theoretical predictions (Herbert 1980, 1983a). A rich review of early results on channel-flow stability can be found in the Ph.D. thesis by Pugh (1988).

Since modal stability theory cannot fully explain the laminar–turbulent transition in fully developed channel flow, attention shifted to nonmodal stability theory (Gustavsson 1991; Reddy & Henningson 1993). A common approach to the nonmodal stability problem is to identify the optimal disturbances that maximise amplification over all possible initial conditions. Butler & Farrell (1992) showed that linearly stable three-dimensional disturbances in fully developed laminar channel flow can undergo transient growth before ultimately decaying. These optimal disturbances were found to have zero streamwise wavenumber and take the form of streamwise vortices, which evolve into streaks of high or low streamwise velocity. Optimal disturbances have also been computed in turbulent channel flows by Butler & Farrell (1993), del Álamo & Jiménez (2006) and Pujals *et al.* (2009).

Experimental observations of transitional and turbulent wall-bounded flows have revealed the existence of coherent structures in the form of organised patterns of vorticity that persist in both time and space. The significance of coherent structures in turbulent transport processes has driven investigations aimed at finding distinct solutions to the Navier-Stokes equations that capture the characteristics of these structures (Graham & Floryan 2021). These solutions are now known as exact coherent structures (ECS). Following the idea of the self-sustained mechanism (Hamilton *et al.* 1995; Waleffe 1997), Waleffe (1998) discovered three-dimensional nonlinear travelling-wave solutions in free-slip plane Poiseuille flow by taking steady states in the free-slip plane Couette flow as starting points. These solutions were later extended to travelling-wave solutions in plane Poiseuille flow by homotopy from free-slip to no-slip boundary conditions (Waleffe 2001, 2003). The plane Poiseuille flow investigated by Waleffe was a half Poiseuille flow with the upper wall corresponding to the centreplane of a full plane Poiseuille flow. The close resemblance between the profiles of half Poiseuille flow and plane Couette flow made the homotopy possible. These solutions are remarkably similar to the coherent structures observed in the near-wall region of fully developed turbulent channel flow and also capture the most important statistical features of turbulence. Other families of ECS in plane Poiseuille flow (e.g., periodic-like, mirror-symmetric, hairpin-like and localised) were found by other researchers (e.g., Toh & Itano 2003; Nagata & Deguchi 2013; Zammert & Eckhardt 2014; Gibson & Brand 2014; Wall & Nagata 2016; Shekar & Graham 2018; Yang *et al.* 2019; Engel *et al.* 2025). Further research work is needed to establish how these structures become unstable and break down to the turbulent regime.

1.2. Channel-entrance flow

The discrepancies between theoretical predictions and experimental observations in fully developed channel flow have drawn attention to the disturbances in the entrance region, as a likely cause of the failure of classical stability theory (Herbert 1984*a,b*). Research efforts first focused on the computation of the velocity and pressure distributions of the laminar entrance flow (Bodoia & Osterle 1961; Sparrow *et al.* 1964; Van Dyke 1970; Fang & Saber 1987; Sadri & Floryan 2002). Building on these studies of the base flow, subsequent investigations turned to its stability characteristics.

Linear stability analysis of symmetric disturbances for a channel-entrance flow was conducted by Hahnemann *et al.* (1948), Chen & Sparrow (1967) and Gupta & Garg (1981*a,b*) under the parallel-flow assumption. The critical Reynolds number was found to decrease monotonically along the channel entrance, eventually approaching the fully developed value. The problem was later generalised to account for non-axisymmetric disturbances (Gupta & Garg 1981*c*) and to incorporate non-parallel flow effects (Garg & Gupta 1981*a,b*). The stabilising character of the channel-entrance flow was also discovered by Biau (2008) in the far downstream region. It is widely accepted that, for a fixed bulk Reynolds number, channel flow is more stable in the entrance region than in the fully developed region.

The stability and transition of the channel-entrance flow have also been examined by taking into account different forms of the imposed disturbances. Duck (2005) investigated the transient growth of three-dimensional disturbances in the entrance region of a channel. The channel boundary layers were perturbed at the mouth by the boundary-layer eigensolutions calculated by Luchini (1996). The bypass transition of the channel-entrance flow was studied by Buffat *et al.* (2014) using direct numerical simulations (DNS). The laminar boundary layer on the upper wall was perturbed by small-amplitude optimal disturbances at a distance of two channel heights from the mouth. Alizard *et al.* (2018) studied the secondary stability of streaks embedded in a channel-entrance flow using a global linear optimisation analysis and DNS. The streamwise-elongated streaks were generated at the lower wall by a pair of optimal streamwise vortices, obtained through linear transient growth analysis.

Although these studies focused on the stability of flow profiles at different streamwise locations in the channel entrance, it is surprising that the receptivity, i.e. how external disturbances excite instability in the entrance region, was not considered. The physical mechanisms by which free-stream vortical disturbances superimposed on the oncoming inviscid flow are entrained into the channel inlet and evolve downstream were therefore not investigated. This problem, however, is of central importance, as even noted by Reynolds (1883), who observed that inlet disturbances significantly influence the stability and laminar-turbulent transition of the pipe entrance flow. By controlling the disturbance level at the pipe inlet, the flow studied by Reynolds (1883) remained laminar at Reynolds numbers, based on the mean flow velocity and the pipe diameter, ranging from 2,000 to 13,000. This number was further extended to 100,000 in the experiments of Pfenniger (1961), where efforts were taken to minimise the disturbance level. For a channel-entrance flow, Nishioka *et al.* (1975) successfully sustained laminar flow up to $Re_c = 8000$ by reducing the turbulence intensity of the oncoming flow to 0.05%. The significant variation of the transitional Reynolds number in these studies highlights the sensitive dependence of the stability and transition of confined flows to the inlet disturbance intensity.

Under the small-amplitude assumption, Ricco & Alvarenga (2021) carried out the first theoretical and numerical study of the entrainment of free-stream vortical disturbances in the channel entrance. Their interest lay in how these disturbances are affected by the channel confinement and how they grow and develop downstream. The perturbation flow at the channel inlet was obtained by a matched asymptotic composite solution between a vortical flow in the core of the channel entrance and boundary-layer perturbation flows developing on the channel walls. Ricco & Alvarenga (2022) and Zhu & Ricco (2024) investigated the linear and nonlinear evolution of vortical disturbances entrained in the entrance region of a pipe, respectively. Good agreement between their velocity profiles and experimental measurements was obtained. Zhu & Ricco (2024) discovered elongated pipe-entrance nonlinear structures (EPENS) characterised by high- and low-speed streaks spanning the whole pipe cross-section. These structures remarkably resemble the nonlinear travelling wave solutions found in fully developed pipe flow (e.g., Wedin & Kerswell 2004; Hof *et al.* 2004).

1.3. Boundary-region framework

A brief overview of the boundary-region framework is presented herein as it is the methodology adopted in this study. The boundary-region equations are parabolised Navier-Stokes equations, in which the streamwise derivatives are neglected in the viscous diffusion and pressure gradient terms. These simplifications follow from the asymptotic limits of low frequency and large Reynolds number. The terminology was first adopted by Kemp (1951) in his study of a flow past a side edge. Leib *et al.* (1999) employed the linearised boundary-region equations, along with appropriate upstream and far-field boundary conditions derived using asymptotic methods, to describe the evolution of disturbances induced by free-

stream turbulence in an incompressible flat-plate boundary layer. The objective was to obtain a rigorous mathematical description of Klebanoff modes, streamwise-elongated boundary-layer structures observed in experiments. In the flat boundary-layer geometry, this mathematical framework was extended to the nonlinear incompressible case by Ricco *et al.* (2011) and to compressible cases by Ricco & Wu (2007) and Marensi *et al.* (2017). The equations have also been used to study vortex–wave interactions (Hall & Smith 1991; Deguchi *et al.* 2013) and Görtler vortices in boundary layers evolving over concave surfaces (Hall 1983, 1988; Wu *et al.* 2011; Marensi & Ricco 2017; Xu *et al.* 2017, 2024). Applications of the boundary-region equations to confined flows include Ravi Sankar *et al.* (1988), Duck (2005) and Song & Deguchi (2025).

As discussed in §1.2, Ricco and coworkers have shown that the boundary-region framework is also useful to investigate the linear and nonlinear development of vortical disturbances entrained in the entrance regions of pipe flows, as well as the linear development of such disturbances in channel flows. This framework is therefore chosen for the channel-flow problem of interest here.

1.4. Objectives of the present study

In this paper, we investigate the entrainment of flow disturbances into the entrance of a channel and the downstream evolution of the induced nonlinear vortical disturbances. The oncoming disturbances are physically realistic, i.e. they can be generated at the channel mouth in a laboratory. The dynamics is governed by the nonlinear incompressible boundary-region equations, applied and solved numerically in the channel-flow geometry.

Our study is the nonlinear extension of Ricco & Alvarenga (2021) and the first theoretical study of the entrainment and downstream evolution of finite-amplitude disturbances in the entrance region of a channel. Our nonlinear results represent a further step towards a complete understanding of the stability and transition to turbulence of confined flows perturbed by realistic entry perturbations. The nonlinear regime follows the entrainment of the oncoming disturbances and the initial small-amplitude growth dictated by the linearised dynamics. Studies of the secondary instability of the nonlinear flow computed in our study and DNS of the fully-fledged transition to turbulence represent important future research directions.

In §2, the scaling and the assumptions are presented, together with the mathematical formulation and the numerical procedures. The numerical results are discussed in §3. A summary and conclusions are given in §4.

2. Mathematical formulation and numerical procedures

2.1. Scaling and flow decomposition

We consider a pressure-driven incompressible channel flow bounded between two infinite parallel flat plates, separated by a distance $2h^*$. A Cartesian coordinate system $\mathbf{x}^* = \{x^*, y^*, z^*\}$ is used to describe the flow, where x^* , y^* and z^* represent the streamwise, wall-normal and spanwise directions, respectively. The channel mouth is located at $x^* = 0$, while the lower and upper plates, assumed to be infinitely thin, are at $y^* = 0$ and $y^* = 2h^*$, respectively. The superscript $*$ indicates dimensional quantities. In this paper, the term “inlet” refers to locations $x^* \ll h^*$, while the term “entrance” refers to the whole streamwise extent of the channel-entrance region. A schematic of the flow is shown in figure 1.

A uniform streamwise flow with velocity U_∞^* is assumed at $x^* = 0$, which serves as an appropriate simplification of the flow approaching two parallel infinitely thin plates. For channels with a sharp-edged mouth, the Jeffery–Hamel solutions (Jeffery 1915; Hamel 1917) can be employed, as demonstrated by Sadri & Floryan (2002). Superimposed on the oncoming

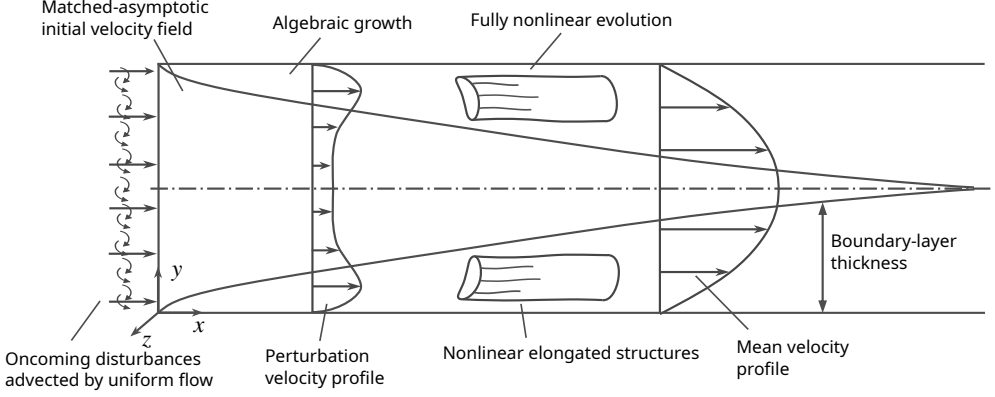


Figure 1: Schematic of the entrance region of the perturbed channel flow (not to scale).

flow are small-amplitude gust-type vortical fluctuations. A pair of vortical modes with the same frequency f^* (and hence the same streamwise wavenumber k_x^*) but opposite spanwise wavenumber k_z^* is considered ($k_z^* \geq 0$ is taken without losing generality). The spanwise wavelength of the free-stream gusts, λ_z^* , is chosen as the reference length. The velocities \mathbf{u}^* and the time t^* are normalised by U_∞^* and λ_z^*/U_∞^* , respectively, while the pressure p^* is normalised by $\rho^*U_\infty^{*2}$, where ρ^* is the density of the fluid.

Our focus is on oncoming disturbances with a long streamwise wavelength (i.e. low frequency), i.e. $k_x \ll 1$, which have been experimentally demonstrated to be the most likely to penetrate into boundary layers and form streamwise-elongated structures (Matsubara & Alfredsson 2001). Following Ricco & Alvarenga (2021), the pair of free-stream gusts passively advected by U_∞^* is expressed as

$$\mathbf{u} - \{1, 0, 0\} = \epsilon \left\{ \hat{\mathbf{u}}_+^\infty e^{ik_z z} + \hat{\mathbf{u}}_-^\infty e^{-ik_z z} \right\} e^{ik_x(x-t)} + \text{c.c.}, \quad (2.1)$$

where

$$\hat{\mathbf{u}}_\pm^\infty = \left\{ \hat{u}_{y_+}^\infty e^{ik_y y} + \hat{u}_{y_-}^\infty e^{-ik_y y}, \hat{v}_{y_+}^\infty e^{ik_y y} + \hat{v}_{y_-}^\infty e^{-ik_y y}, \pm \left(\hat{w}_{y_+}^\infty e^{ik_y y} + \hat{w}_{y_-}^\infty e^{-ik_y y} \right) \right\}, \quad (2.2)$$

$\mathbf{u} = \{u, v, w\}$ are the velocity components in the x , y and z directions, $\epsilon \ll 1$ is a measure of the amplitude of the disturbances, the quantities $\{\hat{u}_{y_\pm}^\infty, \hat{v}_{y_\pm}^\infty, \hat{w}_{y_\pm}^\infty\} = O(1)$ with the subscript y_\pm corresponding to the exponents $\pm ik_y y$, k_y is the wall-normal wavenumber and c.c. denotes the complex conjugate. To preserve the symmetry with respect to the channel centreplane, we choose $k_y = \pi l/h$, $l \in \mathbb{Z}$. Two special cases, $\hat{u}_{y_+}^\infty = \hat{u}_{y_-}^\infty$ and $\hat{u}_{y_+}^\infty = -\hat{u}_{y_-}^\infty$, are considered, producing symmetric and antisymmetric streamwise velocities, respectively. Accordingly, we set $\hat{w}_{y_+}^\infty = \hat{w}_{y_-}^\infty$ for the first case and $\hat{w}_{y_+}^\infty = -\hat{w}_{y_-}^\infty$ for the second case, ensuring that the streamwise and spanwise velocities have the same symmetries, while the wall-normal velocities have opposite symmetries. Similar representations of the free-stream vortical disturbances have been used by Ricco *et al.* (2011) and Marensi *et al.* (2017) for flat-plate boundary layers, Xu *et al.* (2017) and Marensi & Ricco (2017) for concave boundary layers, and Ricco & Alvarenga (2022) and Zhu & Ricco (2024) for pipe flows. The expansion (2.1) is a model of free-stream vortical disturbances that could be realised by a grid of vibrating ribbons in a laboratory, as in the careful receptivity studies of Dietz (1999) and Borodulin *et al.* (2021). Under the low-frequency assumption, the continuity equation of the

gust disturbances becomes

$$\pm k_y \hat{v}_{y_{\pm}}^{\infty} + k_z \hat{w}_{y_{\pm}}^{\infty} = 0, \quad (2.3)$$

where $\partial u / \partial x = O(k_x) \ll 1$ has been neglected.

As the oncoming flow enters the channel, two boundary layers develop on the channel walls and their boundary-layer thickness becomes comparable with the spanwise wavelength of the disturbance at $x = O(Re_{\lambda})$, where $Re_{\lambda} = U_{\infty}^* \lambda_z^* / \nu^* \gg 1$ and ν^* is the kinematic viscosity of the fluid. A distinguished scaling is $k_x = O(Re_{\lambda}^{-1})$ and the two slow variables scaled by k_x are $\bar{t} = k_x t = O(1)$ and $\bar{x} = k_x x = O(1)$. In this region, viscous-diffusion effects in the wall-normal and spanwise directions are comparable. The flow can thus be described by the nonlinear boundary-region equations (Ricco *et al.* 2011), here written and solved in the channel flow framework. The linear counterpart of this problem, formulated for turbulent Reynolds numbers $r_t = \epsilon Re_{\lambda} \ll 1$, was solved in Ricco & Alvarenga (2021) for the case of small-amplitude disturbances. The current research relaxes the linear assumption because $r_t = O(1)$. Nonlinear interactions are thus taken into account.

The governing equations are derived from the incompressible Navier-Stokes equations

$$\nabla \cdot \mathbf{u} = 0, \quad (2.4)$$

$$\frac{\partial \mathbf{u}}{\partial t} + (\mathbf{u} \cdot \nabla) \mathbf{u} = -\nabla p + \frac{1}{Re_{\lambda}} \nabla^2 \mathbf{u}. \quad (2.5)$$

Following Leib *et al.* (1999) and Ricco & Alvarenga (2021), the velocity \mathbf{u} and the pressure p are decomposed into the laminar base flow and the perturbation flow, namely

$$\begin{aligned} \{\mathbf{u}, p\} &= \{\mathbf{U}, P\} + \{\tilde{\mathbf{u}}, \tilde{p}\} \\ &= \{U(\bar{x}, y), k_x V(\bar{x}, y), 0, P(\bar{x})\} + r_t \left\{ \bar{u}, k_x \bar{v}, k_x \bar{w}, \frac{k_x}{Re_{\lambda}} \bar{p} + \Gamma \right\}, \end{aligned} \quad (2.6)$$

where the perturbation flow is expressed as a Fourier series in \bar{t} and z :

$$\{\bar{u}, \bar{v}, \bar{w}, \bar{p}, \Gamma\} = \sum_{m,n=-\infty}^{\infty} \{\hat{u}_{m,n}, \hat{v}_{m,n}, \hat{w}_{m,n}, \hat{p}_{m,n}, \hat{\Gamma}_{m,n}\} e^{im\bar{t} + ink_z z}. \quad (2.7)$$

The pressure correction $\Gamma(\bar{t}, \bar{x}, z)$ ensures that the mass flow rate is conserved at each time instant and at each streamwise location. As the physical quantities are real, the Hermitian property applies, i.e.

$$(\hat{q}_{m,n})_{c.c.} = \hat{q}_{-m,-n}, \quad (2.8)$$

where $\hat{q}_{m,n}$ represents any Fourier coefficient in (2.7).

Substituting (2.6)–(2.7) into the Navier-Stokes equations (2.4)–(2.5) and taking the limits $k_x^{-1}, Re_{\lambda} \rightarrow \infty$ with $\mathcal{F} = k_x Re_{\lambda} = O(1)$ leads to the boundary-layer equations governing the laminar base flow $\{U, V, P\}$ and to the nonlinear unsteady boundary-region equations governing the perturbation flow $\{\hat{u}_{m,n}, \hat{v}_{m,n}, \hat{w}_{m,n}, \hat{p}_{m,n}, \hat{\Gamma}_{m,n}\}$. These equations, supplemented by the appropriate initial and boundary conditions, are presented in §2.2 and §2.3, respectively. This mathematical framework was first developed by Leib *et al.* (1999) to describe the evolution of Klebanoff modes induced by unsteady free-stream disturbances in a pre-transitional flat-plate boundary layer. It was later extended to concave boundary layers, pipe-entrance flows and channel-entrance flows. Instead of k_x , Wu *et al.* (2011) used Re_{λ}^{-1} for scaling in order to investigate steady Görtler vortices evolving in a concave boundary layer. The scaling based on k_x is adopted herein to remain consistent with Ricco & Alvarenga (2021). The mathematical formulation for the development of steady perturbations in a channel is presented in Appendix A, using the scaling based on Re_{λ}^{-1} .

2.2. Governing equations for the base flow

The laminar boundary-layer equations read (Bodoia & Osterle 1961)

$$\frac{\partial U}{\partial \bar{x}} + \frac{\partial V}{\partial y} = 0, \quad (2.9)$$

$$U \frac{\partial U}{\partial \bar{x}} + V \frac{\partial U}{\partial y} = -\frac{dP}{d\bar{x}} + \frac{1}{\mathcal{F}} \frac{\partial^2 U}{\partial y^2}. \quad (2.10)$$

Equations (2.9) and (2.10) are solved together with the condition for the conservation of mass flow rate,

$$\int_0^h U dy = h, \quad (2.11)$$

and are subject to the no-slip and no-penetration conditions at the bottom wall and to the symmetry conditions at the centreplane:

$$y = 0 : \quad U = V = 0, \quad (2.12)$$

$$y = h : \quad \frac{\partial U}{\partial y} = 0, \quad V = 0. \quad (2.13)$$

The initial condition for (2.9) and (2.10) is a composite solution, constructed by matching the near-wall Blasius boundary-layer flow with an inviscid core flow, using the method of matched asymptotic expansions in the region $\bar{x} \ll O(1)$ with $x = O(1)$ (Ricco & Alvarenga 2021). For the lower half of the channel, the initial condition is given by

$$U(x, y) = \frac{dF}{d\eta} + Re_\lambda^{-1/2} \frac{\pi}{2h^2} \left\{ \sin^2 \left(\frac{\pi y}{h} \right) \int_0^\infty \frac{\beta \sqrt{2\sigma} d\sigma}{\{\cosh[\pi(x-\sigma)/h] - \cos(\pi y/h)\}^2} + \right. \\ \left. \cos \left(\frac{\pi y}{h} \right) \int_0^\infty \frac{-\beta \sqrt{2\sigma} d\sigma}{\cosh[\pi(x-\sigma)/h] - \cos(\pi y/h)} - \int_0^\infty \frac{-\beta \sqrt{2\sigma} d\sigma}{\cosh[\pi(x-\sigma)/h] - 1} \right\}, \quad (2.14)$$

where $\eta = y(Re_\lambda/2x)^{1/2}$, $F(\eta)$ satisfies the Blasius equation $F''' + FF'' = 0$, the prime denotes differentiation and $\beta = \lim_{\eta \rightarrow \infty} (\eta - F) = 1.217 \dots$.

2.3. Governing equations for the perturbation flow

The perturbation-flow is governed by the nonlinear unsteady boundary-region equations as follows.

The continuity equation is

$$\frac{\partial \hat{u}_{m,n}}{\partial \bar{x}} + \frac{\partial \hat{v}_{m,n}}{\partial y} + ink_z \hat{w}_{m,n} = 0. \quad (2.15)$$

The x -momentum equation is

$$\underbrace{\left(im + \frac{\partial U}{\partial \bar{x}} + \frac{n^2 k_z^2}{\mathcal{F}} \right) \hat{u}_{m,n}}_{\text{term 1}} + \underbrace{U \frac{\partial \hat{u}_{m,n}}{\partial \bar{x}}}_{\text{term 2}} + \underbrace{V \frac{\partial \hat{u}_{m,n}}{\partial y}}_{\text{term 3}} + \underbrace{\frac{\partial U}{\partial y} \hat{v}_{m,n}}_{\text{term 4}} - \underbrace{\frac{1}{\mathcal{F}} \frac{\partial^2 \hat{u}_{m,n}}{\partial y^2}}_{\text{term 5}} + \underbrace{\frac{d\hat{\Gamma}_{m,0}}{d\bar{x}}}_{\text{term 6}} = \underbrace{r_l \hat{\chi}_{m,n}}_{\text{term 7}}. \quad (2.16)$$

The y -momentum equation is

$$\left(im + \frac{\partial V}{\partial y} + \frac{n^2 k_z^2}{\mathcal{F}} \right) \hat{v}_{m,n} + U \frac{\partial \hat{v}_{m,n}}{\partial \bar{x}} + V \frac{\partial \hat{v}_{m,n}}{\partial y} + \hat{u}_{m,n} \frac{\partial V}{\partial \bar{x}} + \frac{1}{\mathcal{F}} \frac{\partial \hat{p}_{m,n}}{\partial y} - \frac{1}{\mathcal{F}} \frac{\partial^2 \hat{v}_{m,n}}{\partial y^2} = r_t \hat{\mathcal{Y}}_{m,n}. \quad (2.17)$$

The z -momentum equation is

$$\left(im + \frac{n^2 k_z^2}{\mathcal{F}} \right) \hat{w}_{m,n} + U \frac{\partial \hat{w}_{m,n}}{\partial \bar{x}} + V \frac{\partial \hat{w}_{m,n}}{\partial y} + \frac{ink_z}{\mathcal{F}} \hat{p}_{m,n} - \frac{1}{\mathcal{F}} \frac{\partial^2 \hat{w}_{m,n}}{\partial y^2} = r_t \hat{\mathcal{Z}}_{m,n}. \quad (2.18)$$

The numbering of the terms of the x -momentum equation is used in Appendix E. The terms on the right-hand sides of equations (2.16)–(2.18) denote the nonlinear terms

$$\left. \begin{aligned} \hat{\mathcal{X}}_{m,n} &= - \left(\frac{\partial \hat{u}\hat{u}}{\partial \bar{x}} + \frac{\partial \hat{u}\hat{v}}{\partial y} + ink_z \hat{u}\hat{w} \right)_{m,n}, \\ \hat{\mathcal{Y}}_{m,n} &= - \left(\frac{\partial \hat{u}\hat{v}}{\partial \bar{x}} + \frac{\partial \hat{v}\hat{v}}{\partial y} + ink_z \hat{v}\hat{w} \right)_{m,n}, \\ \hat{\mathcal{Z}}_{m,n} &= - \left(\frac{\partial \hat{u}\hat{w}}{\partial \bar{x}} + \frac{\partial \hat{v}\hat{w}}{\partial y} + ink_z \hat{w}\hat{w} \right)_{m,n}, \end{aligned} \right\} \quad (2.19)$$

where $\hat{\cdot}$ indicates Fourier transformed quantities. In the limit $r_t \ll 1$, the linearised boundary-region equations of Ricco & Alvarenga (2021) are recovered. The pressure correction $\hat{\Gamma}_{m,0}$ becomes a further unknown when $n = 0$. One more condition is thus required to solve the system. Analogous to (2.11) for the base-flow problem, the mass flow rate must be conserved at each instant in time and at each streamwise location. As discussed in Appendix B, this condition is expressed as

$$\int_0^{2h} \hat{u}_{m,0} dy = 0. \quad (2.20)$$

Since the partial differential system (2.15)–(2.20) is parabolic in the streamwise direction and elliptic in the wall-normal direction, appropriate initial and boundary conditions are needed. These conditions are presented in §2.3.1. Further treatment of (2.15)–(2.20) is discussed in §2.3.2 for different values of n .

2.3.1. Initial and boundary conditions for the perturbation flow

While the streamwise velocity of the induced disturbances acquires an order-one amplitude at $\bar{x} = O(1)$, the velocity fluctuations at the channel inlet are of small amplitude $O(\epsilon)$ and nonlinear effects can therefore be neglected there. The initial conditions derived by Ricco & Alvarenga (2021) for the linear analysis can thus be used in the region where $\bar{x} \ll O(1)$. These initial conditions are constructed at the channel inlet by matching the outer solution, composed of the oncoming convected gust and the inviscid perturbation arising from rapid distortion theory, with the viscous inner solution emerging from the unsteady boundary-layer equations. Comparison between (2.8) in Ricco & Alvarenga (2021) and the velocity expansions (2.6) leads to the relations

$$\{\hat{u}_{-1,1}, \hat{v}_{-1,1}\} = \frac{1}{Re_\lambda} \left\{ \frac{ik_z}{k_x} \bar{u}_{ic} + \bar{u}_{ic}^{(0)}, \frac{ik_z}{k_x} \bar{v}_{ic} + \bar{v}_{ic}^{(0)} \right\}, \quad (2.21)$$

where \bar{u}_{ic} , $\bar{u}_{ic}^{(0)}$, \bar{v}_{ic} and $\bar{v}_{ic}^{(0)}$ are given by the analytical expressions (3.11)–(3.13) and (3.18) in Ricco & Alvarenga (2021). The spanwise velocity $\hat{w}_{-1,1}$ can be found through the continuity

equation (2.15) with $\hat{u}_{-1,1}$ and $\hat{v}_{-1,1}$ given by (2.21). For the opposite spanwise wavenumber, the same streamwise and wall-normal components but opposite spanwise component are derived:

$$\{\hat{u}_{-1,-1}, \hat{v}_{-1,-1}, \hat{w}_{-1,-1}\} = \{\hat{u}_{-1,1}, \hat{v}_{-1,1}, -\hat{w}_{-1,1}\}. \quad (2.22)$$

The initial conditions for $(m, n) = (1, \pm 1)$ are obtained from the Hermitian property (2.8):

$$\{\hat{u}_{1,\pm 1}, \hat{v}_{1,\pm 1}, \hat{w}_{1,\pm 1}\} = \{\hat{u}_{-1,\mp 1}, \hat{v}_{-1,\mp 1}, \hat{w}_{-1,\mp 1}\}_{c.c.}. \quad (2.23)$$

It also occurs that

$$\hat{u}_{m,n} = \hat{v}_{m,n} = \hat{w}_{m,n} = 0 \quad \text{for } (m, n) \neq (\pm 1, \pm 1). \quad (2.24)$$

Since the streamwise derivative of $\hat{p}_{m,n}$ is negligible in the x -momentum equation (2.16) under the low-frequency assumption, no initial condition for $\hat{p}_{m,n}$ is required. Appendix C shows contours of the initial velocity perturbations for two cases and discusses the differences from the initial conditions used in previous studies.

In the wall-normal direction, equations (2.15)–(2.20) are subject to the no-slip and no-penetration conditions at the walls ($y = 0$ and $y = 2h$):

$$\hat{u}_{m,n} = \hat{v}_{m,n} = \hat{w}_{m,n} = 0. \quad (2.25)$$

For the numerical procedures discussed in §2.4, only the initial and boundary conditions for Fourier modes with nonnegative indices n are required, since we impose the Hermitian property along the z direction.

2.3.2. Initial-boundary-value problems for the perturbation flow

For convenience of the numerical calculations, the nonlinear boundary-region equations (2.15)–(2.20), together with the initial conditions (2.21)–(2.24) and the boundary conditions (2.25), are solved in different forms according to the value of n .

For the components with $n \neq 0$, the pressure $\hat{p}_{m,n}$ and the spanwise velocity $\hat{w}_{m,n}$ can be eliminated from (2.15)–(2.19) as in Ricco & Alvarenga (2021). The resulting equations read

$$\left(im + \frac{\partial U}{\partial \bar{x}} + \frac{n^2 k_z^2}{\mathcal{F}} \right) \hat{u}_{m,n} + U \frac{\partial \hat{u}_{m,n}}{\partial \bar{x}} + V \frac{\partial \hat{u}_{m,n}}{\partial y} + \frac{\partial U}{\partial y} \hat{v}_{m,n} - \frac{1}{\mathcal{F}} \frac{\partial^2 \hat{u}_{m,n}}{\partial y^2} = r_t \hat{\mathcal{X}}_{m,n}, \quad (2.26)$$

$$\begin{aligned} & \mathcal{V} \hat{v}_{m,n} + \mathcal{V}_y \frac{\partial \hat{v}_{m,n}}{\partial y} + \mathcal{V}_x \frac{\partial \hat{v}_{m,n}}{\partial \bar{x}} + \mathcal{V}_{yy} \frac{\partial^2 \hat{v}_{m,n}}{\partial y^2} + \mathcal{V}_{yyy} \frac{\partial^3 \hat{v}_{m,n}}{\partial y^3} + \mathcal{V}_{xyy} \frac{\partial^3 \hat{v}_{m,n}}{\partial \bar{x} \partial y^2} + \\ & \mathcal{V}_{yyy} \frac{\partial^4 \hat{v}_{m,n}}{\partial y^4} + \mathcal{U} \hat{u}_{m,n} + \mathcal{U}_x \frac{\partial \hat{u}_{m,n}}{\partial \bar{x}} + \mathcal{U}_{yy} \frac{\partial^2 \hat{u}_{m,n}}{\partial y^2} + \mathcal{U}_{xy} \frac{\partial^2 \hat{u}_{m,n}}{\partial \bar{x} \partial y} \\ & = r_t \frac{\partial^2 \hat{\mathcal{X}}_{m,n}}{\partial \bar{x} \partial y} + r_t n^2 k_z^2 \hat{\mathcal{Y}}_{m,n} + ink_z r_t \frac{\partial \hat{\mathcal{Z}}_{m,n}}{\partial y}, \end{aligned} \quad (2.27)$$

where the coefficients $\mathcal{V}, \mathcal{V}_y, \mathcal{V}_x, \dots, \mathcal{U}_{xy}$ are given in Appendix D. A similar framework was used for the DNS of a turbulent channel flow (Kim *et al.* 1987) and for the solution of the Orr–Sommerfeld equations (Schmid & Henningson 2001). In this case, only the initial and boundary conditions for $\{\hat{u}_{m,n}, \hat{v}_{m,n}\}$ are needed. The initial conditions are given in (2.21)–(2.24) and the boundary conditions are

$$\hat{u}_{m,n} = \hat{v}_{m,n} = \frac{\partial \hat{v}_{m,n}}{\partial y} = 0, \quad \text{at } y = 0, 2h. \quad (2.28)$$

The last condition in (2.28) is obtained by inserting $\hat{u}_{m,n} = \hat{w}_{m,n} = 0$ from (2.25) into the continuity equation (2.15). The spanwise velocity $\hat{w}_{m,n}$ can be obtained a posteriori from

the continuity equation. The pressure $\hat{p}_{m,n}$ can be calculated either from the y -momentum equation (2.17) or from the z -momentum equation (2.18) once $\hat{w}_{m,n}$ is found.

For the components with $n = 0$, the pressure $\hat{p}_{m,0}$ only appears in the y -momentum equation (2.17). The three velocity components $\{\hat{u}_{m,0}, \hat{v}_{m,0}, \hat{w}_{m,0}\}$ and the pressure correction $\hat{\Gamma}_{m,0}$ are obtained by solving the continuity, x - and z -momentum equations,

$$\frac{\partial \hat{u}_{m,0}}{\partial \bar{x}} + \frac{\partial \hat{v}_{m,0}}{\partial y} = 0, \quad (2.29)$$

$$\left(im + \frac{\partial U}{\partial \bar{x}} \right) \hat{u}_{m,0} + U \frac{\partial \hat{u}_{m,0}}{\partial \bar{x}} + V \frac{\partial \hat{u}_{m,0}}{\partial y} + \frac{\partial U}{\partial y} \hat{v}_{m,0} - \frac{1}{\mathcal{F}} \frac{\partial^2 \hat{u}_{m,0}}{\partial y^2} + \frac{d\hat{\Gamma}_{m,0}}{d\bar{x}} = r_t \hat{\mathcal{X}}_{m,0}, \quad (2.30)$$

$$im \hat{w}_{m,0} + U \frac{\partial \hat{w}_{m,0}}{\partial \bar{x}} + V \frac{\partial \hat{w}_{m,0}}{\partial y} - \frac{1}{\mathcal{F}} \frac{\partial^2 \hat{w}_{m,0}}{\partial y^2} = r_t \hat{\mathcal{Z}}_{m,0}, \quad (2.31)$$

together with (2.20) for the conservation of the mass flow rate, as discussed in §2.1. The initial and boundary conditions for (2.29)–(2.31) are given in (2.24) and (2.25). The pressure $\hat{p}_{m,0}$ is computed a posteriori from the y -momentum equation (2.17).

2.4. Numerical procedures

For the base flow, equations (2.9)–(2.11), supplemented by conditions (2.12)–(2.14), are solved by an improved version of the numerical scheme of Bodoia & Osterle (1961). A detailed description of the numerical procedures is found in §2.4 of Ricco & Alvarenga (2021). The numerical results are further discussed in the supplementary material S2 of Ricco & Alvarenga (2021).

For the perturbation flow, the initial-boundary-value problems described in §2.3.2 are solved by an integration method in the streamwise direction. The governing equations are discretised by second-order finite-difference schemes employing a one-sided backward uniform grid along \bar{x} and a central-difference uniform grid along y . The discretised system of the components with $n \neq 0$ forms a block tridiagonal matrix and is solved at each \bar{x} location by a standard block tridiagonal matrix algorithm (Cebeci 2002). For the system of components with $n = 0$, the composite trapezoidal rule is used for the calculation of the integral (2.20) and a staggered grid is used in the y direction to reduce the ill-conditioning of the matrix of the discretised system. Since the velocity components and the pressure gradient are computed simultaneously, the block tridiagonal structure of the matrix is lost. A modified block tridiagonal matrix algorithm is used to solve this system (refer to Appendix C of Zhu & Ricco (2024)).

The computation of the nonlinear terms on the right-hand sides of the momentum equations given in (2.19) is evaluated using a predictor-corrector method at each \bar{x} location. In the predictor step, the initial approximation of the nonlinear terms uses the results at the previous \bar{x} location to treat the discretised nonlinear system explicitly as a linear algebra system. The velocity computed from the predictor step is used to improve the initial guess in the corrector step. This iteration is repeated until a convergence criterion is fulfilled. An under-relaxation method is used to accelerate this procedure. At each iteration, the nonlinear terms are calculated using the pseudo-spectral method, in which the Fourier coefficients of the velocity components are first transformed to the physical space to carry out the multiplications. The products are then transformed back to the spectral space. The aliasing error is eliminated by employing the 3/2 rule, which avoids the spurious energy cascade from the unresolved high-frequency modes into the resolved low-frequency ones. As the Hermitian property (2.8) is applied along the z direction, only the Fourier modes with nonnegative indices n need to be calculated. The modes with negative n indices are evaluated through (2.8). The

Fourier series is truncated at $m = \pm N_t$ and $n = \pm N_z$ for the frequency and the spanwise wavenumber, respectively. Resolution checks show that the use of $N_t = N_z = 16$, with grid sizes $\Delta \bar{x} = 0.001$ and $\Delta y = 0.004h$, is sufficient to capture the nonlinear effects induced by the free-stream forcing modes (2.1) for the cases presented in §3.

3. Results

3.1. Scaling and flow parameters

In §2, the spanwise wavelength of the gust λ_z^* is utilised as the reference length in order to relate our asymptotic analysis to the boundary-layer flow analysis of Leib *et al.* (1999) and to the linear analysis of Ricco & Alvarenga (2021). The numerical results are instead presented in terms of quantities rescaled by the half-channel height h^* , except for the coordinate z^* and time t^* , which are rescaled by their respective wavenumbers to express them in terms of π . It follows that $\mathbf{u} = \mathbf{u}(x_h, y_h, \bar{z}, \bar{t}; Re_h, k_{x,h}, k_{y,h}, k_{z,h}, \hat{u}_{y_{\pm}}^{\infty}, \hat{v}_{y_{\pm}}^{\infty}, \hat{w}_{y_{\pm}}^{\infty})$, where $(x_h, y_h) = (x^*, y^*)/h^*$, $Re_h = U_{\infty}^* h^* / \nu^*$, $(k_{x,h}, k_{y,h}, k_{z,h}) = (k_x^*, k_y^*, k_z^*) h^*$, $\bar{z} = k_z^* z^*$ and \bar{t} is defined in §2. The quantities scaled by λ_z^* and h^* are related as $(x, y) = h(x_h, y_h)$, $Re_{\lambda} = Re_h / h$, $(k_x, k_y, k_z) = (k_{x,h}, k_{y,h}, k_{z,h}) / h$, where $h = h^* / \lambda_z^*$.

Linear stability analysis of the channel-entrance flow predicts that the critical Reynolds number decreases monotonically with the streamwise distance from the mouth, approaching the value for the fully developed regime in the downstream limit (Hahnemann *et al.* 1948; Chen & Sparrow 1967; Gupta & Garg 1981*a,b,c*; Garg & Gupta 1981*a,b*). However, experimental observations have reported transition at Reynolds numbers lower than this theoretical limit (Patel & Head 1969; Kao & Park 1970; Carlson *et al.* 1982), revealing the intrinsic subcritical nature of transition and the importance of accounting for nonlinear effects. We thus focus on the nonlinear evolution of disturbances in the parameter space $k_{x,h} \ll 1$ and $1000 < Re_h < 3500$, where Tollmien–Schlichting waves are not present but algebraic growth of perturbations and transition to turbulence have been observed in experiments.

Unless otherwise indicated, we investigate the nonlinear evolution of disturbances that, at the channel inlet, are symmetric ($\hat{u}_{y_{\pm}}^{\infty} = 1, \hat{v}_{y_{\pm}}^{\infty} = \mp 1, \hat{w}_{y_{\pm}}^{\infty} = 1$) or antisymmetric ($\hat{u}_{y_{\pm}}^{\infty} = \pm 1, \hat{v}_{y_{\pm}}^{\infty} = -1, \hat{w}_{y_{\pm}}^{\infty} = \pm 1$) about the centreplane. With these values assigned to $\hat{v}_{y_{\pm}}^{\infty}$ and $\hat{w}_{y_{\pm}}^{\infty}$, the relation between the wall-normal and spanwise wavenumbers, $k_y = k_z$ (i.e. $k_{y,h} = k_{z,h}$), can be obtained using (2.3). The intensity of the disturbances is monitored by the root mean square (r.m.s.) of the streamwise velocity fluctuations (Pope 2000, p. 687),

$$u_{rms} = r_t \left(\sum_{m=-N_t}^{N_t} \sum_{n=-N_z}^{N_z} |\hat{u}_{m,n}|^2 \right)^{1/2}, \quad m \neq 0. \quad (3.1)$$

The free-stream disturbance intensity is defined as $Tu = \sqrt{(2/3)\mathcal{E}^{gust}}$, where the kinetic energy $\mathcal{E}^{gust} = (|\tilde{u}|^2 + |\tilde{v}|^2 + |\tilde{w}|^2) / 2$ and the velocity components $\{\tilde{u}, \tilde{v}, \tilde{w}\}$ of free-stream gusts are defined in (2.1). For our choice of $\hat{u}_{y_{\pm}}^{\infty}$, $\hat{v}_{y_{\pm}}^{\infty}$ and $\hat{w}_{y_{\pm}}^{\infty}$, $Tu = 2\sqrt{2}\epsilon$.

3.2. Effect of flow parameters

Figure 2 shows the nonlinear streamwise development of the maximum u_{rms} (coloured lines), i.e. $u_{rms,max} = \max_{y_h} u_{rms}$, for symmetric and antisymmetric inlet disturbances and $\epsilon = 0.001, 0.003, 0.005, 0.009$ (i.e. $Tu \approx 0.28\%, 0.85\%, 1.41\%, 2.56\%$). The linear results are rescaled by the corresponding ϵ value and displayed by the grey lines. The linear and nonlinear solutions overlap when the amplitude of the oncoming disturbance is small ($\epsilon = 0.001$) due to weak nonlinear interactions, whereas nonlinear effects become more pronounced as ϵ

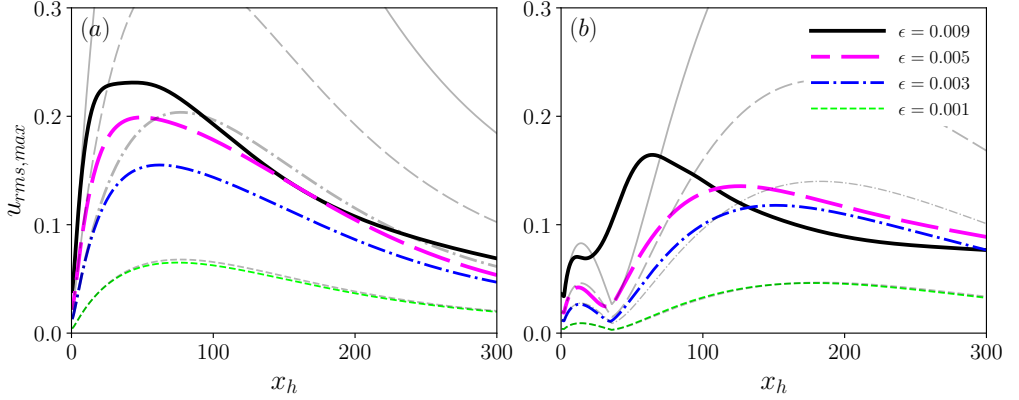


Figure 2: Coloured lines: nonlinear streamwise development of $u_{rms,max}$. Grey lines: linear solutions rescaled by the corresponding ϵ value. Parameters: $Re_h = 1500$, $k_{x,h} = 0.005$, $k_{y,h} = k_{z,h} = \pi$. Panel (a): symmetric inlet disturbances. Panel (b): antisymmetric inlet disturbances.

increases. Nonlinearity causes the peak value to occur further upstream. The perturbation flow generated by symmetric disturbances exhibits an intense initial growth followed by a downstream decay. The perturbation flow produced by antisymmetric disturbances instead experiences a weak initial growth, a temporary decay, a more intense growth downstream and a decay that is more gradual than in the symmetric case. The maximum amplitude of the nonlinear solutions is much lower than that of the corresponding linear ones for both symmetric and antisymmetric cases, indicating the stabilising effect of nonlinearity and the over-prediction of the linear results. The stabilising effect of nonlinearity has already been noted, for example, for streaks in boundary layers (Ricco *et al.* 2011), for elongated structures in the pipe-flow entrance region (Zhu & Ricco 2024) and for Görtler vortices in boundary layers over concave walls (Hall 1988; Marensi & Ricco 2017; Xu *et al.* 2024).

The disturbance amplitudes remain substantial far downstream, even when the base flow becomes independent of the streamwise direction. For example, when $\epsilon = 0.005$, $u_{rms,max}$ reaches 0.07 and 0.1 at $x_h = 265.2$ for the perturbation flow triggered by symmetric and antisymmetric inlet disturbances, respectively. Here, $x_h = 265.2$ is the location where the laminar channel flow becomes fully developed at $Re_h = 1500$ (Durst *et al.* 2005). For $\epsilon = 0.009$, the perturbation flow triggered by antisymmetric inlet disturbance persists downstream, with $u_{rms,max}$ saturating to 0.077. In contrast, pipe-flow disturbances at comparable Reynolds numbers and entry-flow conditions exhibit a more intense attenuation after reaching their maximum. They become negligible when the flow has reached fully developed conditions (refer to figure 3 of Zhu & Ricco (2024)). In all the cases, the wall-normal and spanwise velocity components are much smaller than the streamwise velocity component, except very near the channel inlet.

The effect of the Reynolds number Re_h on the streamwise development of $u_{rms,max}$ is displayed in figure 3. For the symmetric cases, a more intense growth is observed at higher Re_h , while farther downstream $u_{rms,max}$ at different Re_h decay at nearly the same rate. The overlap of profiles at the channel inlet in the symmetric case indicates that the initial disturbance growth is independent of Re_h . For the antisymmetric case, after the initial oscillation, the disturbance reaches a peak value of around 0.14 at any Re_h and decays more slowly as Re_h increases.

Figure 4 displays the effect of the streamwise wavenumber on the downstream evolution

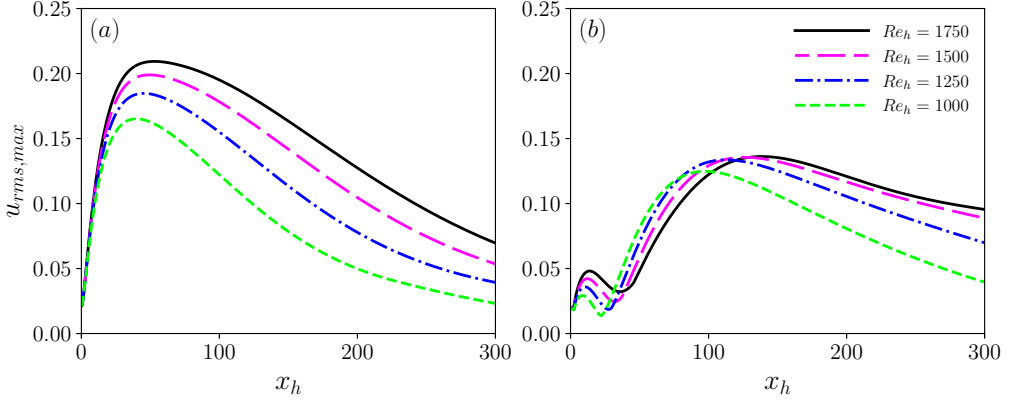


Figure 3: Effect of the Reynolds number Re_h on the streamwise development of $u_{rms,max}$. Parameters: $\epsilon = 0.005$, $k_{x,h} = 0.005$, $k_{y,h} = k_{z,h} = \pi$. Panel (a): symmetric inlet disturbances. Panel (b): antisymmetric inlet disturbances.

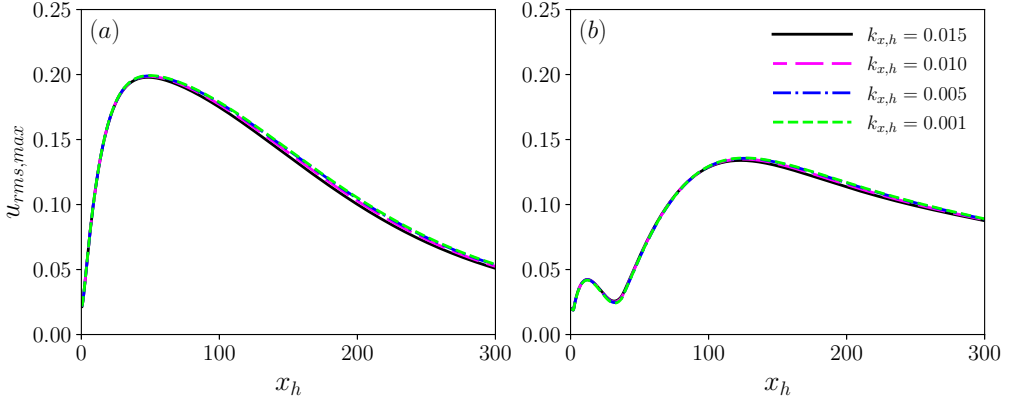


Figure 4: Effect of the streamwise wavenumber $k_{x,h}$ on the streamwise development of $u_{rms,max}$. Parameters: $\epsilon = 0.005$, $Re_h = 1500$, $k_{y,h} = k_{z,h} = \pi$. Panel (a): symmetric inlet disturbances. Panel (b): antisymmetric inlet disturbances.

of $u_{rms,max}$. For $k_{x,h}$ ranging from 0.001 to 0.015, the profiles for both the symmetric and antisymmetric cases overlap, i.e. the nonlinear evolution is independent of the streamwise wavenumber within this range. The independence of the development of the disturbances from small streamwise wavenumbers has also been reported for boundary layer flows (Ricco *et al.* 2011) and pipe flows (Zhu & Ricco 2024).

The wall-normal wavenumber is chosen as $k_{y,h} = l\pi$, with $l \in \mathbb{Z}$, to ensure the symmetry of the inlet disturbances with respect to the centreplane, as discussed in §2. Therefore, the minimum wavenumber is $k_{y,h} = k_{z,h} = \pi$. Figure 5 shows how the change of the wall-normal and spanwise wavenumbers affects the downstream development of $u_{rms,max}$. For wavenumbers larger than π , the profiles of $u_{rms,max}$ in the symmetric case initially increase significantly along the streamwise direction and then decrease to zero. A larger wavenumber results in an earlier peak location, a smaller peak value and a faster attenuation rate, due to the more intense viscous diffusion effects along the wall-normal and spanwise directions. In the most energetic case, i.e. for $k_{y,h} = k_{z,h} = \pi$, the downstream decay is more gradual and the disturbances persist farther downstream than the less energetic cases. For

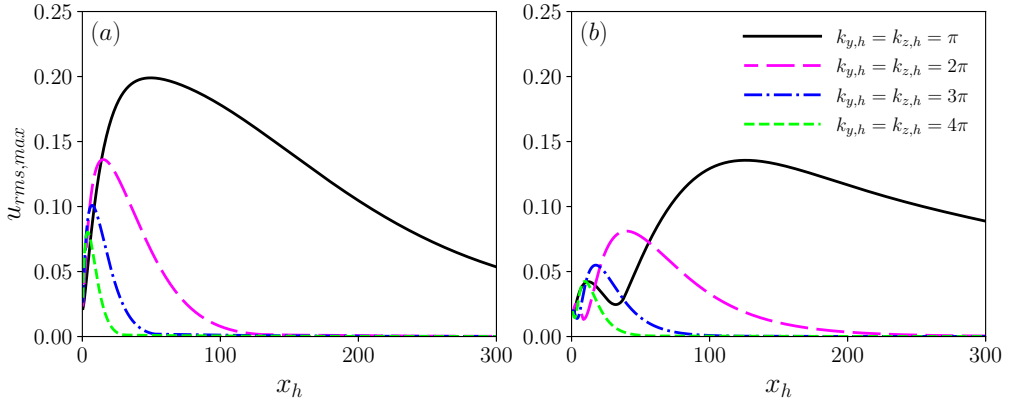


Figure 5: Effect of the wall-normal wavenumber $k_{y,h}$ and spanwise wavenumber $k_{z,h}$ on the streamwise development of $u_{rms,max}$. Parameters: $\epsilon = 0.005$, $Re_h = 1500$, $k_{x,h} = 0.005$. Panel (a): symmetric inlet disturbances. Panel (b): antisymmetric inlet disturbances.

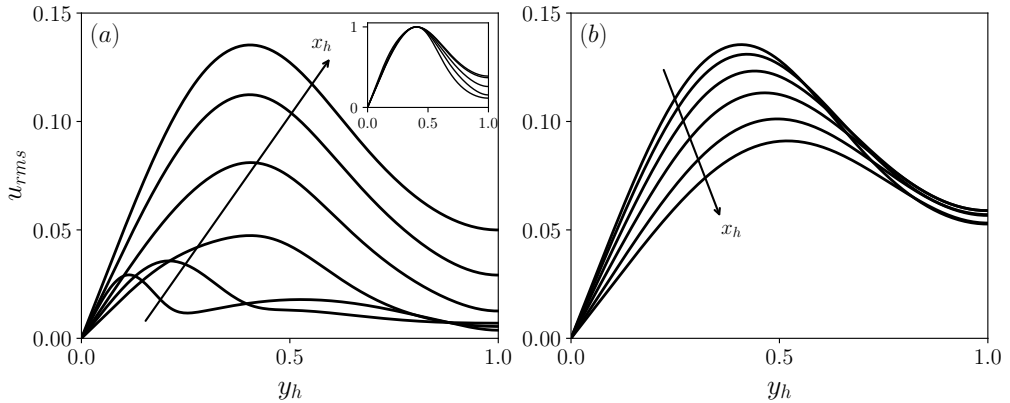


Figure 6: Profiles of u_{rms} at different streamwise locations for the antisymmetric case. Panel (a): growing u_{rms} at $x_h = 4, 20, 45, 60, 80, 120$. Panel (b): decaying u_{rms} at $x_h = 130, 155, 180, 210, 250, 290$. Arrows indicate increasing x_h . The inset shows the profiles of $u_{rms}/u_{rms,max}$ at $x_h = 45, 60, 80, 120, 130$.

the antisymmetric case, after the initial oscillation, the influence of the wavenumbers on the streamwise evolution of the profiles is similar to that observed in the symmetric case.

3.3. Results for a representative case

The representative antisymmetric case for $\epsilon = 0.005$ (i.e. $Tu \approx 1.41\%$), $Re_h = 1500$, $k_{x,h} = 0.005$, $k_{y,h} = k_{z,h} = \pi$ is analysed further because the amplitude of the perturbations remains substantial in the downstream region and displays only a small viscous decay. Figure 6 shows the profiles of u_{rms} at different streamwise locations. The profiles are presented only for $y_h \in [0, 1]$ due to their symmetry about the centreplane. The amplitude of u_{rms} increases with x_h up to $x_h = 127$, after which a monotonic decrease occurs downstream. The peak position of u_{rms} is close to the walls for locations near the channel inlet. It moves towards the centreplane up to $x_h = 45$, after which it is fixed at $y_h = 0.4$ up to $x_h = 130$. The inset of figure 6(a) show that the scaled profiles $u_{rms}/u_{rms,max}$ at $x_h = 45, 60, 80, 120, 130$ collapse

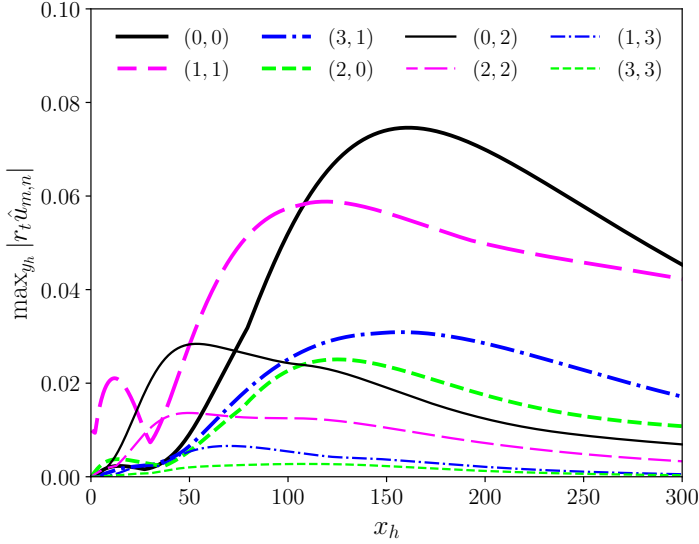


Figure 7: Streamwise development of $\max_{y_h} |r_t \hat{u}_{m,n}|$ for the forcing mode $(m,n) = (1,1)$ and the nonlinearly generated modes for the antisymmetric case.

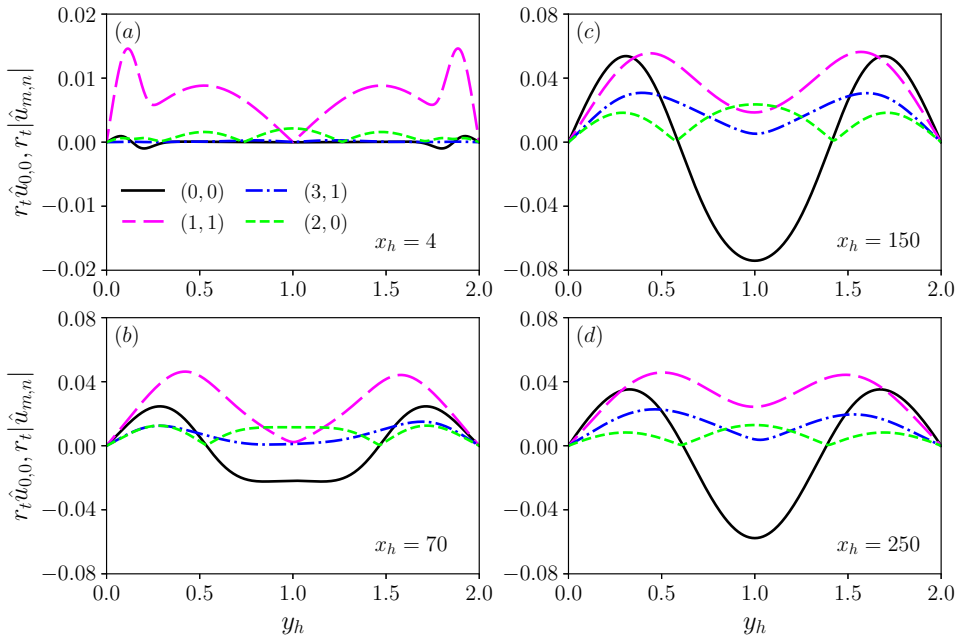


Figure 8: Streamwise velocity profiles of the forcing modes $(m,n) = (1,1)$ and the nonlinearly generated modes at four streamwise locations $x_h = 4, 70, 150, 250$ for the antisymmetric case.

on one another at y locations between the wall and the peak values. When the u_{rms} decays, the peaks shift towards the centreplane. This behaviour differs from that of boundary-layer and pipe flows, for which the peak location of u_{rms} continuously moves away from the wall. A significant disturbance growth is also obtained in the region close to the channel core, where

the base flow is largely inviscid. This growth does not occur in the linearised case where the disturbances decay (refer to figure 10 of Ricco & Alvarenga (2021)). The amplitudes of v_{rms} and w_{rms} are comparable with that of u_{rms} close to the channel inlet, while downstream they become two orders of magnitude smaller than that of u_{rms} after considerable attenuation (not shown).

Figure 7 shows the streamwise development of $\max_{y_h} |r_t \hat{u}_{m,n}|$, the maximum value of $|r_t \hat{u}_{m,n}|$ over y_h at each x_h location, for the forcing mode $(m, n) = (1, 1)$ and the nonlinearly generated modes. For the assumed free-stream disturbances (2.1), modes (m, n) and $(-m, n)$ have the same amplitude and so do modes (m, n) and $(-m, -n)$ because of the Hermitian property (2.8). Therefore, without losing generality, only the results for $m \geq 0$ and $n \geq 0$ are presented in figure 7. An initial oscillation is observed for most of the modes, the most intense one given by the forcing mode $(1, 1)$. The mean-flow distortion $(0, 0)$ acquires significant growth shortly downstream of the channel inlet, grows past the forcing mode $(1, 1)$ at $x_h = 108$ and becomes dominant downstream. After reaching their peak values, all modes experience slow attenuation downstream. Most modes maintain significant amplitudes downstream of $x_h = 265.2$, the entrance length of the laminar channel flow at $Re_h = 1500$ (Durst *et al.* 2005). For instance, the forcing mode $(1, 1)$ and the mean-flow distortion $(0, 0)$ retain 76% and 73% of their respective peak values at this location. This feature is unique for channel flow: in the pipe flow case studied by Zhu & Ricco (2024), all modes decay to zero sufficiently downstream due to viscous effects, following the initial growth. At the streamwise location corresponding to the entrance length of pipe flow and for similar flow conditions, the same modes retain only 4% and 13% of their respective peak values (refer to figure 6 of Zhu & Ricco (2024)).

Figure 8 shows the streamwise velocity profiles of the mean-flow distortion $r_t \hat{u}_{0,0}$, the forcing mode $r_t |\hat{u}_{1,1}|$ and the higher harmonics $r_t |\hat{u}_{2,0}|$ and $r_t |\hat{u}_{3,1}|$ at four different streamwise locations, $x_h = 4, 70, 150, 250$. These four modes retain the strongest magnitudes downstream, as shown in figure 7. The ordinate axis in figure 8(a) is stretched by a factor of four for clarity. At a short distance from the channel mouth ($x_h = 4$), the dynamics is dictated by the forcing mode $r_t |\hat{u}_{1,1}|$, which dominates over the other modes. Farther downstream, the disturbances permeate the entire cross section and the amplitude of all four modes increases before experiencing a gradual attenuation. Downstream of the initial development, the positive mean-flow distortion $r_t \hat{u}_{0,0}$ always exists near the channel wall, while the negative $r_t \hat{u}_{0,0}$ appears near the channel core. This result indicates that the distorted mean flow $\bar{U} = U + r_t \hat{u}_{0,0}$, the sum of the laminar base flow and the mean-flow distortion, exhibits a steeper slope near the channel walls compared to the laminar base flow, while maintaining a smaller magnitude near the channel core. An increase in wall-shear stress results from the nonlinear interactions. Appendix E further discusses the dynamics of the most energetic modes.

3.4. Streamwise elongated structures

3.4.1. Structures generated by antisymmetric inlet disturbances

The instantaneous velocity fields of the perturbation flow $\{\tilde{u}, \tilde{v}, \tilde{w}\}$, defined in (2.6) with respect to the laminar base flow, are shown in figure 9 in (y_h, \bar{z}) planes at $x_h = 4, 50, 100, 150, 200, 250$ and $\bar{t} = 0$ for the antisymmetric case studied in §3.3. The velocity fields at different time instants display similar features to those at $\bar{t} = 0$. The velocity contours of the corresponding initial conditions are shown in figure 27 in Appendix C. Figure 9 visualises the formation and evolution of elongated channel-entrance nonlinear structures (ECENS). Following the use of the acronym EPENS in Zhu & Ricco (2024), the terminology ECENS is adopted to distinguish these structures from streaks that appear in

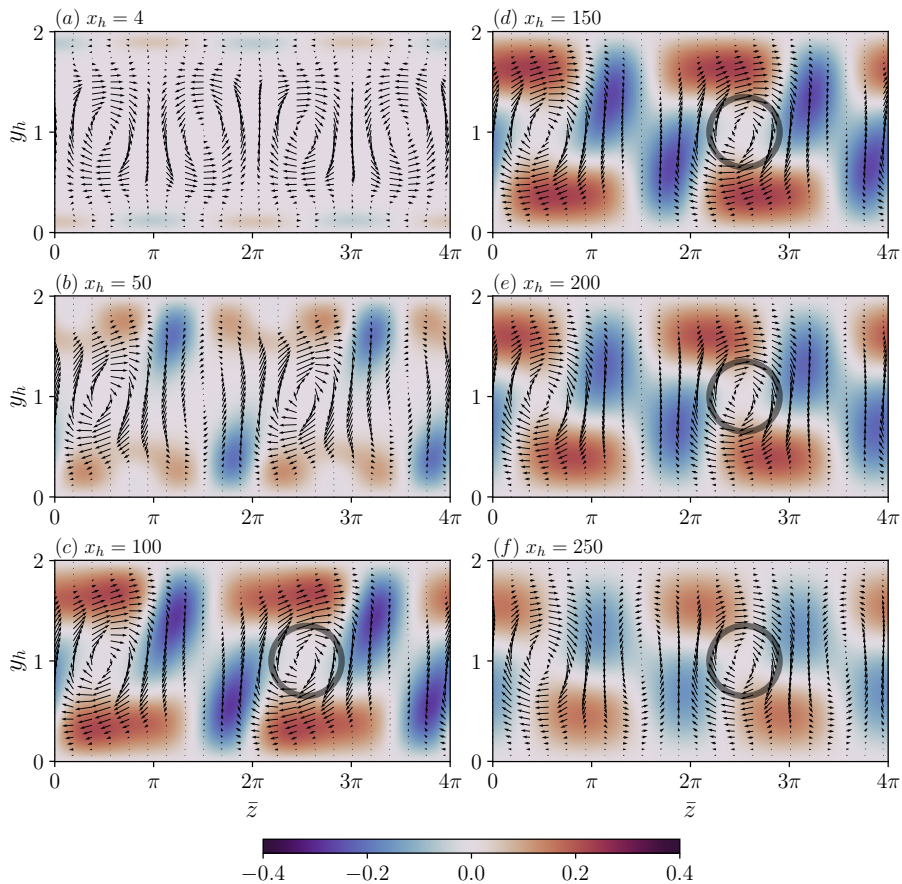


Figure 9: Velocity fields of the perturbation flow $(\tilde{u}, \tilde{v}, \tilde{w})$, triggered by antisymmetric inlet disturbances, in (y_h, \bar{z}) planes at $x_h = 4, 50, 100, 150, 200, 250$ and $\bar{t} = 0$. Here and in the following figures, the brown/blue coloured shading indicates the positive/negative streamwise velocity \tilde{u} . The cross-section vectors $\tilde{v}\mathbf{j} + \tilde{w}\mathbf{k}$ (where \mathbf{j} and \mathbf{k} are unit vectors in the wall-normal and spanwise directions) are indicated by arrows. The streamwise vortices are highlighted by circles. Parameters: $\epsilon = 0.005$, $Re_h = 1500$, $k_{x,h} = 0.005$, $k_{y,h} = k_{z,h} = \pi$.

other contexts, such as Klebanoff modes in flat-plate boundary layers or elongated structures persisting downstream of small roughness elements in laminar boundary layers. At the channel inlet, the three velocity components are of comparable magnitude, i.e. $O(10^{-2})$. The streamwise velocity component \tilde{u} increases downstream and stabilises at $O(10^{-1})$, while the wall-normal and spanwise velocity components, \tilde{v} and \tilde{w} , gradually decrease to $O(10^{-3})$ along the channel.

In contrast to the nonlinear streaks observed in transitional boundary-layer flows (Matsubara & Alfredsson 2001), which are confined to the viscous layer, these elongated structures extend beyond the boundary layers and rapidly occupy the entire cross-section. The effect of nonlinearity is to disrupt the pattern of boundary-layer low-speed and high-speed regions that are equally spaced along the spanwise direction at the channel inlet. The high-speed regions of the ECENS mostly occur near the wall further downstream, while low-speed regions of the ECENS are observed from the walls to the centreplane. This nonlinear effect was also reported for optimal perturbations by Buffat *et al.* (2014) in their figure

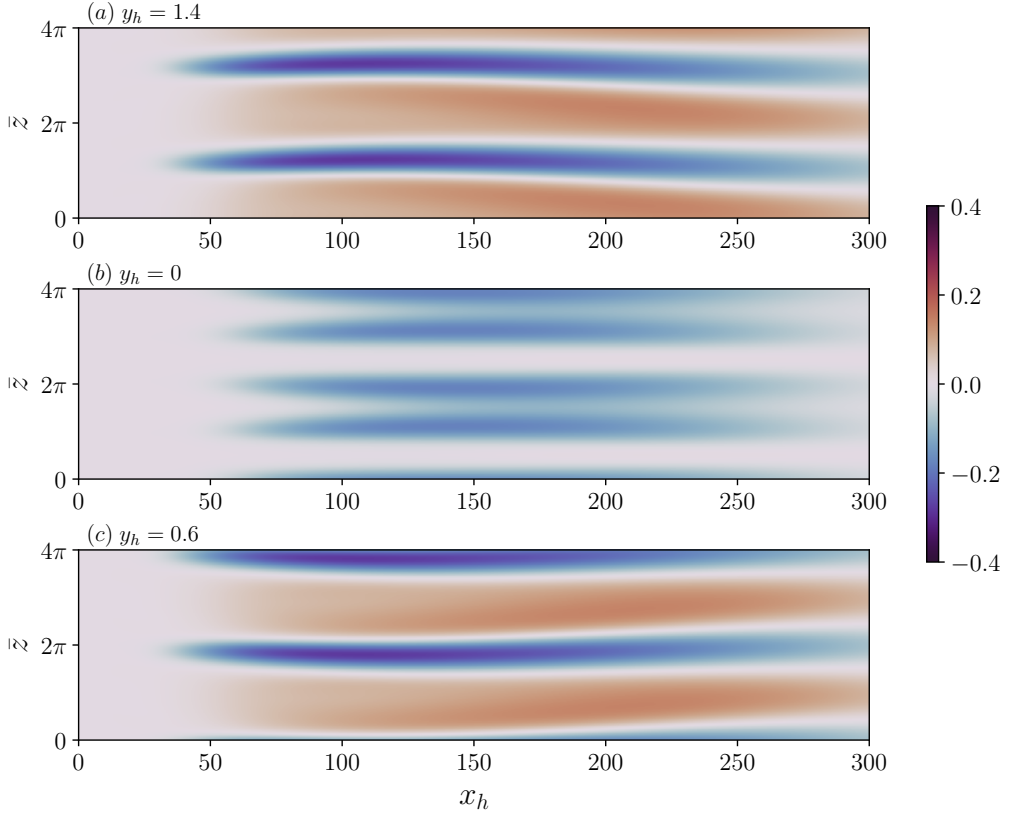


Figure 10: Contours of the streamwise velocity components \tilde{u} , triggered by antisymmetric inlet disturbances, in (x_h, \bar{z}) planes at $y_h = 1.4, 1, 0.6$ and $\bar{t} = 0$. The parameters are the same as those in figure 9.

5, although their perturbation flow does not extend to the centreplane. The antisymmetry of the disturbances at the channel inlet with respect to the centreplane is preserved at $x_h = 4$, but it is disrupted downstream where the ECENS are formed. The ECENS are characterised by streamwise vortical structures, visualised by the cross-section velocity vectors. These streamwise vortices, highlighted by the circles in figures 9(c)–(f), are centred at $y_h = 1$ and located at a spanwise distance $\Delta\bar{z} = 2\pi$ from each other. They persist for a very long streamwise distance and form between two low-speed regions and two high-speed regions of equal size. The ECENS possess a half-turn rotational symmetry, i.e. they are invariant under a rotation of 180 degrees with respect to the centres of the streamwise vortices (x, y_c, z_c) , located at the centreplane: $\tilde{u}(x, y, z) = \tilde{u}(x, 2y_c - y, 2z_c - z)$, $\{\tilde{v}, \tilde{w}\}(x, y, z) = -\{\tilde{v}, \tilde{w}\}(x, 2y_c - y, 2z_c - z)$.

Figure 10 shows the contours of the streamwise velocity components \tilde{u} in (x_h, \bar{z}) planes at $y_h = 1.4, 1, 0.6$ for the same parameters as in figure 9. The low-speed and high-speed regions emerge at around $x_h = 40$, they are streamwise stretched and they meander mildly in the streamwise direction. The low-speed regions are narrower along the spanwise direction than the high-speed regions at $y_h = 1.4$ and 0.6 , while at $y_h = 0$ only low-speed regions are observed. The rotational symmetry observed in the (y_h, \bar{z}) planes is also noted by comparing figures 10(a) and 10(c).

Figure 11 displays the contours of \tilde{u} triggered by the antisymmetric inlet disturbances with

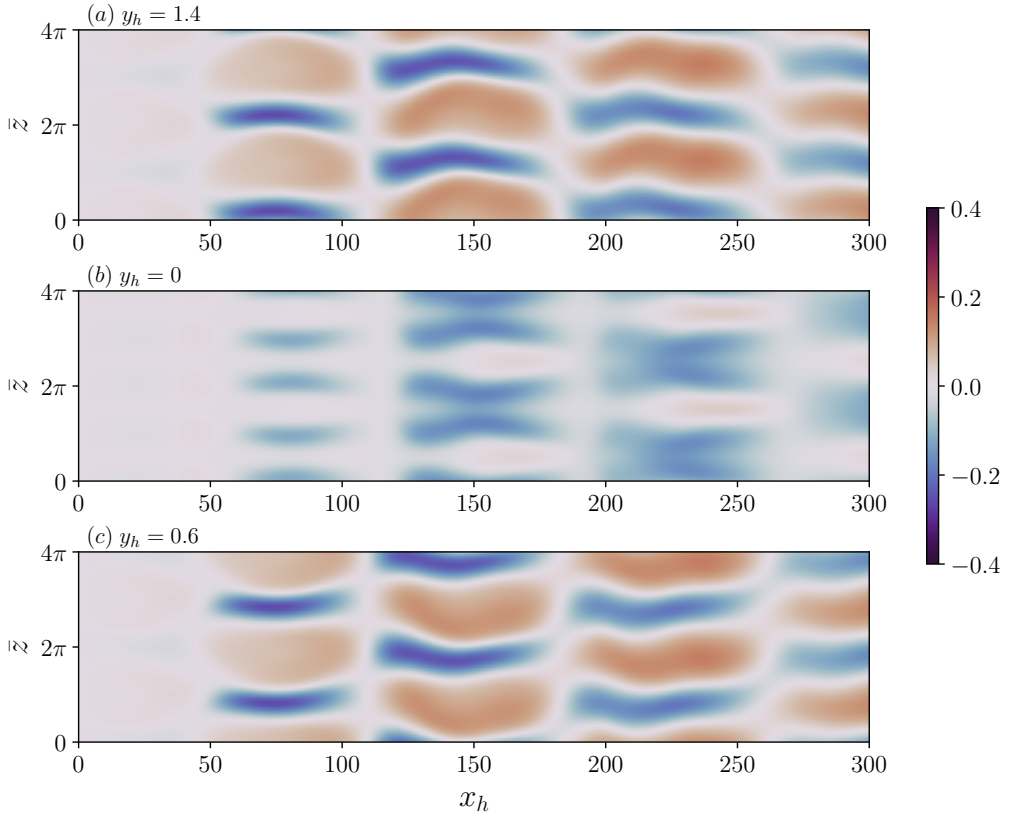


Figure 11: Contours of the streamwise velocity components \tilde{u} , triggered by antisymmetric inlet disturbances in (x_h, \bar{z}) planes at $y_h = 1.4, 1, 0.6$ and $\bar{t} = 0$. Parameters: $\epsilon = 0.005$, $Re_h = 1500$, $k_{x,h} = 0.05$, $k_{y,h} = k_{z,h} = \pi$.

streamwise wavenumber $k_{x,h} = 0.05$, which is ten times larger than that of figure 10. The ECENS exhibit a much shorter streamwise characteristic length for this wavenumber, with the structures featuring a repeating staggered pattern in the streamwise direction. The velocity contours of the ECENS in (y_h, \bar{z}) planes closely resemble those in figure 9 (not shown). Therefore, varying $k_{x,h}$ primarily influences the streamwise distribution of the ECENS, while having minimal impact on their character in (y_h, \bar{z}) planes.

It is worth investigating the effect of the inlet amplitude ϵ on the ECENS. The flow fields generated by less intense inlet disturbances, i.e. $\epsilon = 0.003$, are qualitatively similar to those shown in the preceding figures for $\epsilon = 0.005$, the major quantitative difference is the lower velocity amplitudes. As evident from the contours in figure 12, doubling the inlet amplitude to $\epsilon = 0.01$ has a significant effect on the ECENS near the channel inlet, while sufficiently downstream the ECENS exhibit the same features as shown in panels (e) and (f) of figures 9 and 12. The corresponding contours of \tilde{u} in (x_h, \bar{z}) planes, shown in figure 13, reveal that the ECENS meander along x_h much more when ϵ is larger.

3.4.2. Structures generated by symmetric inlet disturbances

The velocity fields triggered by symmetric inlet disturbances are shown in figures 14 and 15. The velocity contours of the corresponding initial conditions are shown in figure 28 in Appendix C. In contrast to the antisymmetric case in figure 9, the low-speed and high-speed

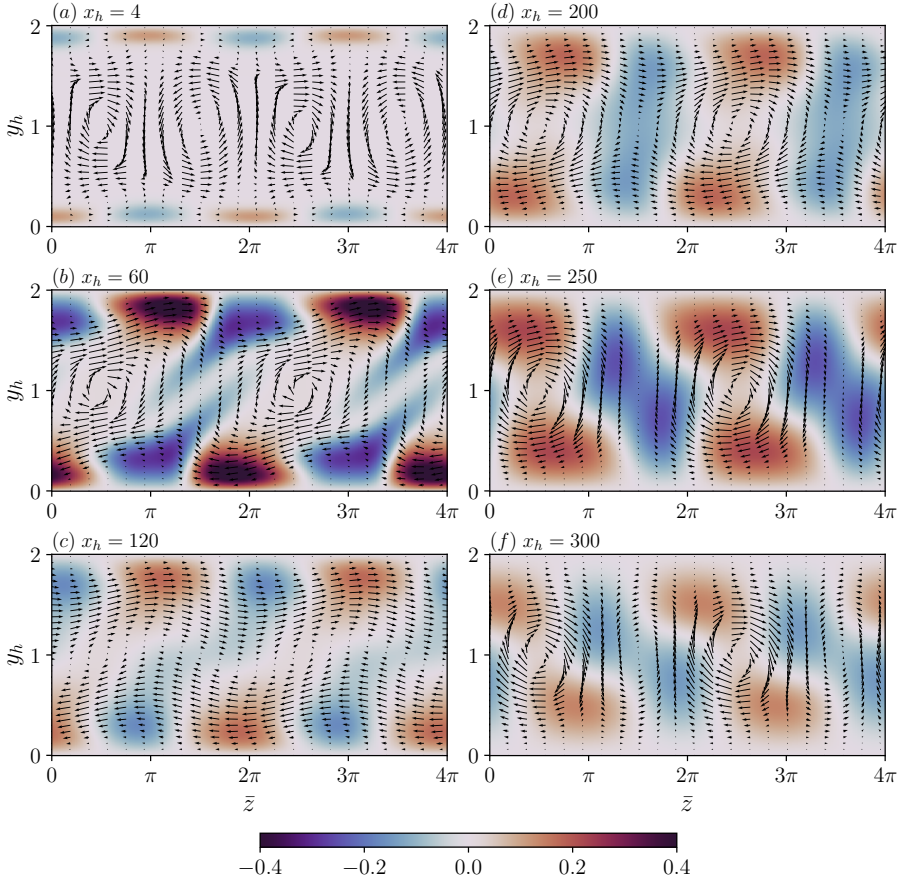


Figure 12: Velocity fields of the perturbation flow $(\bar{u}, \bar{v}, \bar{w})$, triggered by antisymmetric inlet disturbances, in (y_h, \bar{z}) planes at $x_h = 4, 60, 120, 200, 250, 300$ and $\bar{t} = 0$.

Parameters: $\epsilon = 0.01$, $Re_h = 1500$, $k_{x,h} = 0.005$, $k_{y,h} = k_{z,h} = \pi$.

regions in the symmetric case are located near the channel walls for a long streamwise stretch, up to $x_h = 50$, and they alternate along the spanwise direction. The ECENS exhibit a quasi-symmetry about the centreplane at any streamwise location. As the flow progresses downstream ($x_h \geq 100$), the low-speed regions move towards the centreplane and eventually merge. The high-speed regions slightly shift along the spanwise direction, do not merge at the centreplane and they remain separated there. Streamwise vortices form between the low-speed and high-speed regions, but their core is initially not at the centreplane as in the antisymmetric case. These vortices coalesce downstream into a larger vortex located at the centreplane, as highlighted by the circles in figure 14. Comparing figure 10 and figure 15 reveals that the low-speed and high-speed regions meander less when triggered by symmetric inlet disturbances.

Figure 16 shows that an increment of the inlet disturbance to $\epsilon = 0.01$ causes the symmetrical structures at the channel inlet to distort significantly downstream and to develop an antisymmetric character with respect to the centreplane (refer to figures 16(e) and (f)). At those streamwise locations, the ECENS possess a rotational symmetry at the centres of the vortices located at the centreplane, analogous to the ECENS triggered by antisymmetric inlet disturbances (refer to figures 9 and 12). Similar to figure 13, the ECENS visualised in

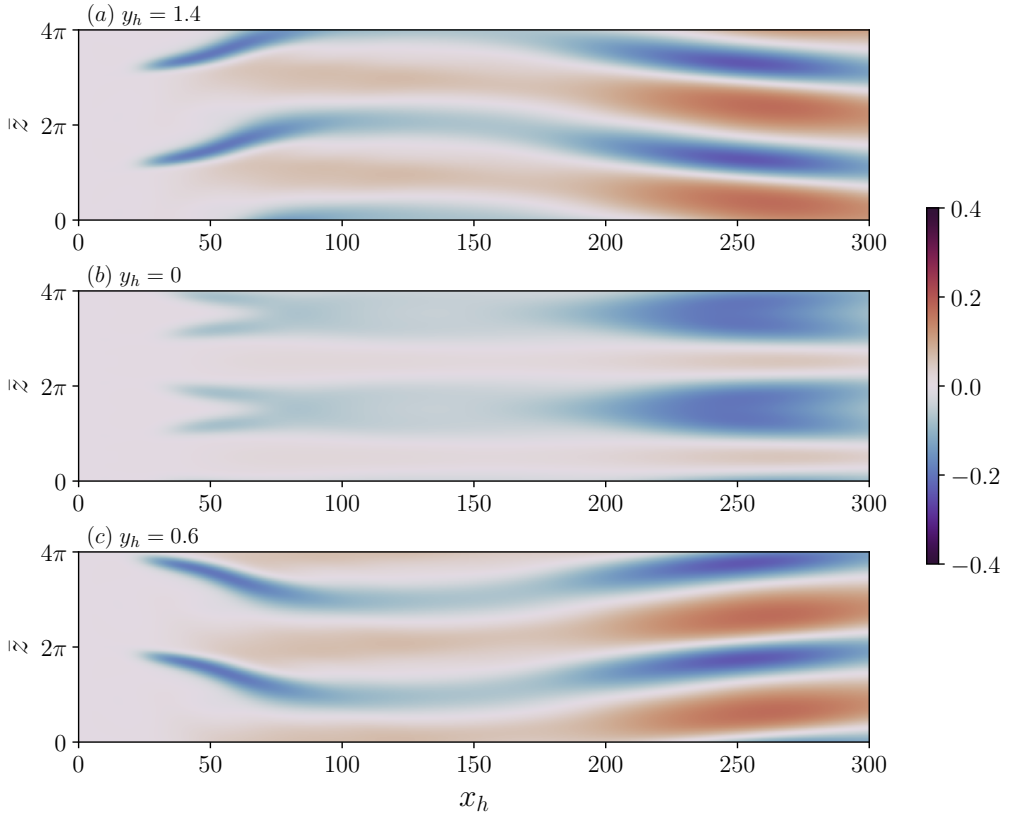


Figure 13: Contours of the streamwise velocity components \tilde{u} , triggered by antisymmetric inlet disturbances in (x_h, \bar{z}) planes at $y_h = 1.4, 1, 0.6$ and $\bar{t} = 0$. The parameters are the same as those in figure 12.

(x_h, \bar{z}) planes meander more along the streamwise direction as the amplitude increases to $\epsilon = 0.01$. These behaviours suggest that the ECENS develop as a nonlinear attractor when nonlinearity is sufficiently intense, as increasing ϵ progressively reduces the dependence of their qualitative features on the spatial distribution of the inlet disturbance.

3.5. Evidence of travelling waves

The contours of the streamwise velocity component at successive time instants reveal that the perturbation flow can have a travelling-wave character. We define the following criteria for identifying travelling waves from numerical data:

- (i) The relative change of maximum root-mean-square velocity $u_{rms,max}$ over 50 half-channel heights is smaller than 5%.
- (ii) The correlation coefficient between matched snapshots at different time instants is larger than 0.95.
- (iii) The relative error of phase speeds is smaller than 5%.

For the second criterion, a snapshot in the (y_h, \bar{z}) plane is chosen as a reference at fixed x_h and \bar{t} . For another time instant \bar{t} , the correlation coefficient is computed between snapshots of the reference flow and flows at different x_h . The snapshot with the largest correlation coefficient is considered a match and is accepted if the coefficient exceeds 0.95. Once two accepted matching snapshots are identified at two time instants, the phase speed can be

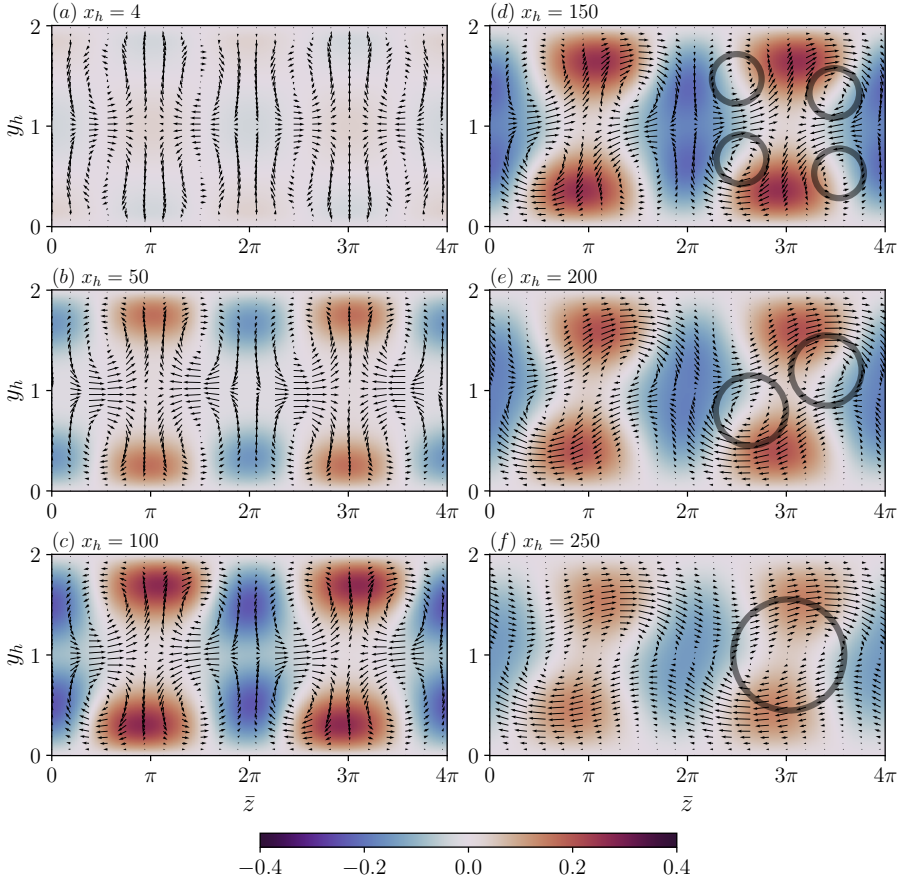


Figure 14: Velocity fields of the perturbation flow $(\tilde{u}, \tilde{v}, \tilde{w})$, triggered by symmetric inlet disturbances in (y_h, \bar{z}) planes at $x_h = 4, 50, 100, 150, 200, 250$ and $\bar{t} = 0$. Parameters: $\epsilon = 0.005$, $Re_h = 1500$, $k_{x,h} = 0.005$, $k_{y,h} = k_{z,h} = \pi$.

calculated as $c = k_x \Delta x_h / \Delta \bar{t}$, where Δx_h and $\Delta \bar{t}$ denote the streamwise displacement and time interval between two snapshots, respectively. A linear fit is performed on the phase speeds computed from multiple snapshot pairs to obtain a robust estimate. The relative error associated with the phase speed of each pair is subsequently calculated and used to evaluate the third criterion.

Based on these three criteria, travelling waves are detected for several parameter combinations. All of them are triggered by antisymmetric inlet disturbances. We here present the results for the case with $\epsilon = 0.009$ (i.e. $Tu \approx 2.55\%$), $Re_h = 1500$, $k_{x,h} = 0.015$, $k_{y,h} = k_{z,h} = \pi$. Figure 17 shows the nonlinear development and persistence of $u_{rms,max}$ along the streamwise direction. The shaded red region indicates the streamwise range $x_h \in [199, 281]$, where the relative change of $u_{rms,max}$ within any interval of 50 half-channel heights is smaller than 5%, satisfying the first criterion. It is worth noting that this region comprises both the entrance region and the fully developed region (the entrance length for the laminar flow is $x_h = 265.2$ at $Re_h = 1500$ (Durst *et al.* 2005)).

Figure 18 displays contours of the streamwise velocity component \tilde{u} in (x_h, \bar{z}) planes at $y_h = 1.4$, plotted at sixteen equally spaced instants over one time period. Shortly downstream of the initial evolution, the perturbation flow develops a travelling-wave character. To identify

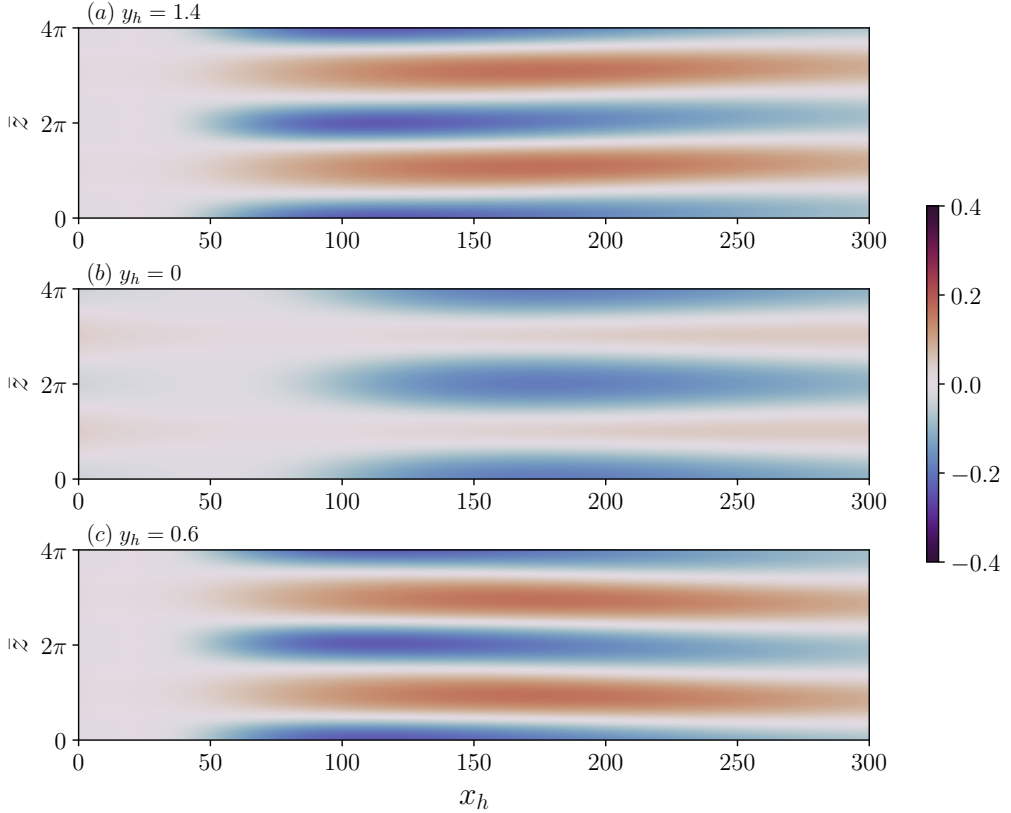


Figure 15: Contours of the streamwise velocity components \tilde{u} , triggered by symmetric inlet disturbances, in (x_h, \bar{z}) planes at $y_h = 1.4, 1, 0.6$ and $\bar{t} = 0$. The parameters are the same as those in figure 14.

matched snapshots between $x_h = 199$ and 281 at different time instants, we selected the snapshot at $x_h = 232$ and $\bar{t} = 21\pi/32$, where the velocity amplitude is relatively large. Following the second criterion, the streamwise locations of matched snapshots are found at different \bar{t} with the correlation coefficient larger than 0.95. The streamwise displacement Δx_h and the time interval $\Delta \bar{t}$ relative to the reference (open circle) are plotted in figure 19. A linear fit (blue line) gives a slope 77.03, corresponding to a phase speed $c = 2.31$. The relative error falls below 5%, satisfying the third criterion.

Figure 20 shows the contours of the streamwise velocity components \tilde{u} of the travelling waves identified within the range $199 < x_h < 281$ in the left panels at four equally spaced time instants. The black lines in panels (a)–(d) indicate the x_h locations of the corresponding velocity fields in the (y_h, \bar{z}) planes shown in the right column. The contour plots display almost identical velocity distributions.

3.6. Comparison with previous studies

3.6.1. Comparison with numerical and theoretical studies

It is worth discussing further how the ECENS studied herein compare with the EPENS discovered by Zhu & Ricco (2024) in the entrance region of a pipe. Similar to the ECENS, the EPENS are elongated along the streamwise direction, they are dominated by the streamwise velocity component and occupy the whole cross-section of the pipe. The EPENS exhibit a

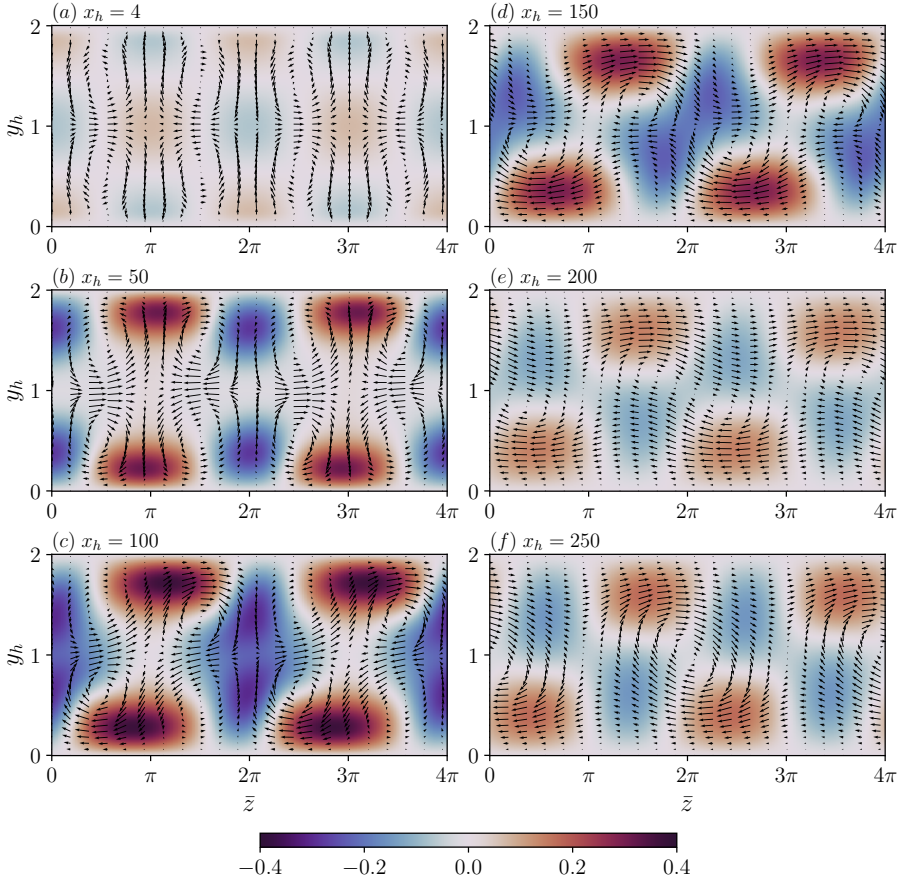


Figure 16: Velocity fields of the perturbation flow $(\tilde{u}, \tilde{v}, \tilde{w})$, triggered by symmetric inlet disturbances, in (y_h, \bar{z}) planes at $x_h = 4, 50, 100, 150, 200, 250$ and $\bar{t} = 0$. Parameters: $\epsilon = 0.01$, $Re_h = 1500$, $k_{x,h} = 0.005$, $k_{y,h} = k_{z,h} = \pi$.

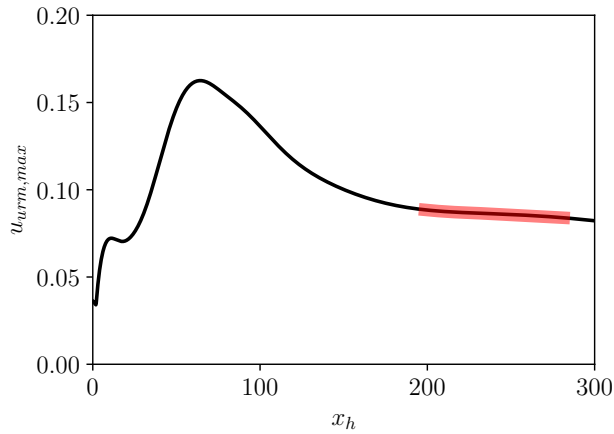


Figure 17: Nonlinear streamwise development of $u_{rms,max}$. The shaded red region indicates the streamwise range $x_h \in [199, 281]$, where the relative change of $u_{rms,max}$ within any interval of 50 half-channel heights is less than 5%.

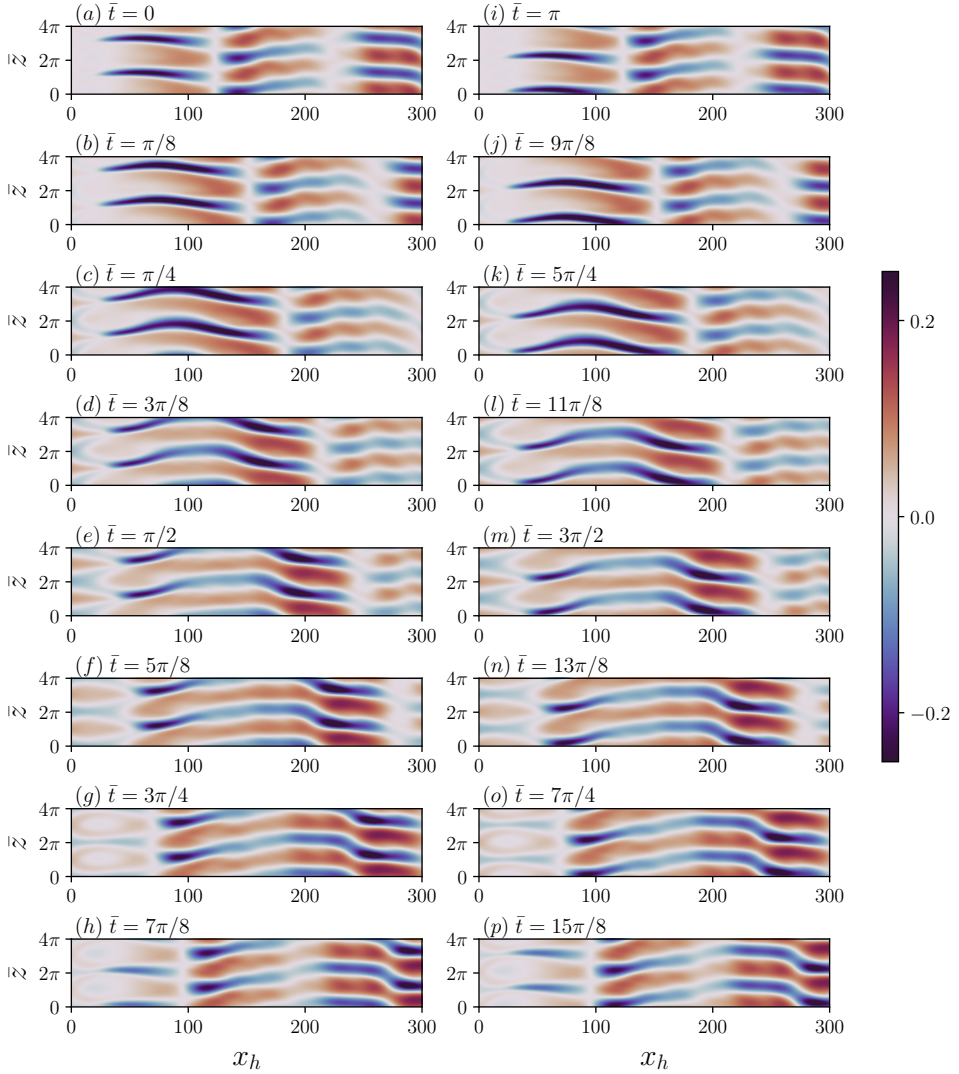


Figure 18: Contours of streamwise velocity component \tilde{u} of the perturbation flow in (x_h, \bar{z}) planes at $y_h = 1.4$ and equally spaced time instants.

rotational symmetry similar to the ECENS, with high-speed regions positioned near the wall and low-speed regions centred around the pipe core. They closely resemble the ECS found numerically and observed experimentally in fully developed pipe flow. The potential use of EPENS as initial guesses for the numerical search of ECS was suggested.

In fully developed channel flow, various families of ECS have been discovered (e.g., Waleffe 1997; Toh & Itano 2003; Nagata & Deguchi 2013; Zammert & Eckhardt 2014; Gibson & Brand 2014; Wall & Nagata 2016; Shekar & Graham 2018; Yang *et al.* 2019; Engel *et al.* 2025). Among these ECS solutions, the so-called TW3 solution identified by Wall & Nagata (2016) possesses a half-turn rotational symmetry about a streamwise axis passing through a point on the channel centreplane, analogous to the ECENS. Figure 21 reproduces figures 7(c) and 7(d) of Wall & Nagata (2016), where two velocity fields of TW3 in (y_W, z_W) planes are shown. The nondimensional variables y_W and z_W correspond to those of figure 7 in Wall

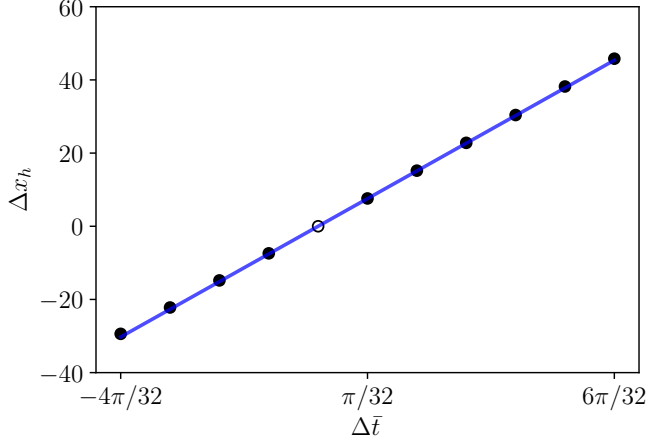


Figure 19: Plot of streamwise displacement Δx_h against time interval $\Delta \bar{t}$. The open cycle denotes the reference with $\Delta x_h = \Delta \bar{t} = 0$. The blue line indicates the linear fit with slope 77.03, corresponding to a phase speed of $c = 2.31$.

& Nagata (2016). The similarity with ECENS (figures 20(e)–(h)) is evident. Both structures feature a low-speed streak near the centreplane and a high-speed streak near the wall in each half of the channel. The main difference lies in the alignment of the upper-half and lower-half high-speed streaks: in TW3 they are aligned in the spanwise direction, whereas in ECENS they are shifted. Although ECENS arise in the channel-entrance region, their persistence into the fully developed region suggests a possible connection with TW3.

Identifying ECS requires substantial numerical effort because they require good initial guesses, whereas ECENS can be computed efficiently with our approach. We thus propose the use of ECENS as initial guesses in the search for new families of ECS in fully developed channel flow. These computations can be achieved by using ECENS at a given time instant as initial conditions for DNS.

The theoretical predictions of Sadri & Floryan (2002) and the experimental measurements of Asai & Floryan (2004) are also of interest. By linearised dynamics, Sadri & Floryan (2002) studied the channel-entrance flow where the distortion of the laminar base flow decayed to a small amplitude compared with that of the fully developed Poiseuille flow. Asai & Floryan (2004) reported that the theoretical profile of Sadri & Floryan (2002) matched well the experimental data of the perturbation flow. Motivated by this finding, we have compared our numerical results with the theory of Sadri & Floryan (2002). Figure 22(a) presents the normalised streamwise velocity deviation of the laminar base flow from the laminar Poiseuille flow, $(U - U_p)/(U_c - U_{p,c})$, where U_p denotes the laminar Poiseuille velocity and the subscript c denotes quantities at the centreplane. The theoretical curve is reproduced from figure 5 of Asai & Floryan (2004). The three streamwise positions x_h correspond to the measurement locations of Asai & Floryan (2004). Our numerical data exhibit an excellent match in the case where the perturbations decay downstream and the Poiseuille profile is recovered. A remarkable agreement is also obtained with their experimental data (not shown here for brevity). Figure 22(b) shows that our profiles of the normalised mean flow distortion $\hat{u}_{0,0}/\hat{u}_{0,0,c}$ also agree with the theoretical profile very well.

3.6.2. Comparison with experimental studies

In this section, we present a comparison between our numerical results and the experimental measurements reported by Nishioka *et al.* (1975) and Asai & Nishioka (1989). In the nu-

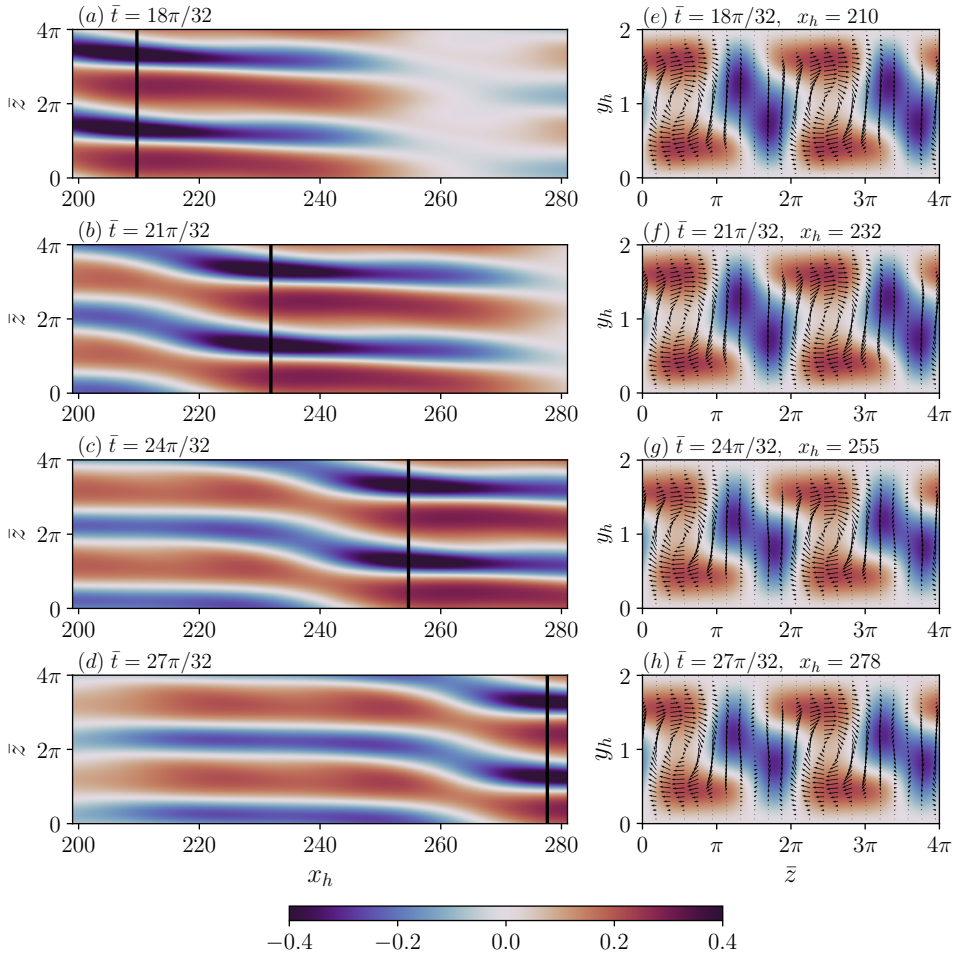


Figure 20: Left panels: contours of the streamwise velocity component \tilde{u} of the perturbation flow in (x_h, \bar{z}) planes at $y_h = 1.4$ for $\bar{t} = 18\pi/32, 21\pi/32, 24\pi/32$ and $27\pi/32$. Right panels: velocity fields, $(\tilde{u}, \tilde{v}, \tilde{w})$, in (y_h, \bar{z}) planes, plotted at the streamwise locations indicated by the black line in the corresponding left panels.

merical simulations, parameters are selected to match the experimental conditions whenever available. For parameters not explicitly reported, values are adjusted to reproduce the main trends observed in the experiments. It is noted that variations in these parameters have a negligible effect on the overall shape of the resulting profiles.

An experimental study was conducted by Nishioka *et al.* (1975) in a rectangular channel with an aspect ratio of 27.4. Most of their reported disturbances were generated by a vibrating ribbon located close to the lower wall and in the fully developed region. Only figures 2 and 3 in Nishioka *et al.* (1975) show velocity profiles evolving without artificial excitation, as in the present study. Figure 23 compares the centreplane streamwise velocity along the spanwise direction measured in their experiments (reproduced in panel (a)) with our numerical results (panel (b)). The dimensional variables $U_{N,c}^*$ and z_N^* correspond to those of figure 2 in Nishioka *et al.* (1975), while $u_{str}^* = U_\infty^* (U + r_t \sum_n \hat{u}_{0,n} e^{in\bar{z}})$, i.e. the time-averaged velocity. From bottom to top, panel (a) shows the velocity profiles with increasing Re_c , the Reynolds number based on the centreline velocity measured at $z_N^* = 6.5\text{cm}$. The numerical simulations

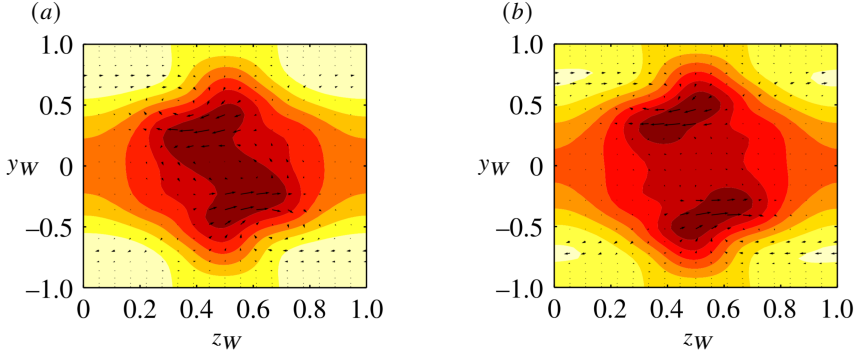


Figure 21: Velocity fields of TW3 discovered by Wall & Nagata (2016). Panel (a): the upper-branch flow (figure 7(c) of Wall & Nagata (2016)). Panel (b): the lower-branch flow (figure 7(d) of Wall & Nagata (2016)). The yellow/red colour shading represents the positive/negative streamwise velocity.

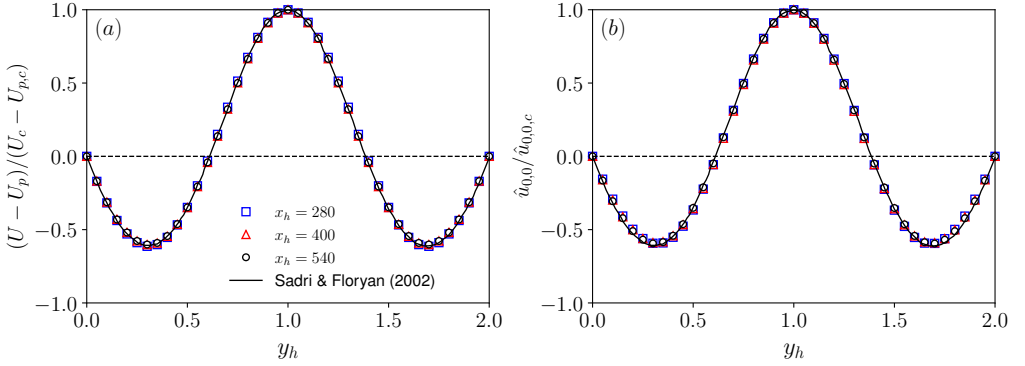


Figure 22: Comparison between the theoretical predictions by Sadri & Floryan (2002) (lines) and our numerical results (symbols) at the same Reynolds number. Panel (a): the normalised streamwise velocity deviation of the laminar base flow from the laminar Poiseuille flow, $(U - U_p)/(U_c - U_{p,c})$. Panel (b): normalised mean flow distortion, $\hat{u}_{0,0}/\hat{u}_{0,0,c}$. Our simulation is performed at $Re_h = 4000$, $\epsilon = 0.001$, $k_{x,h} = 0.005$ and $k_{y,h} = k_{z,h} = 3\pi$, and the results are presented at every 10 numerical steps.

are performed at the corresponding $Re_h = 2Re_c/3$. Both panels (a) and (b) report a wavy velocity distortion along the spanwise direction. This distortion intensifies with increasing Reynolds number, while its shape is largely unchanged.

Asai & Nishioka (1989) also reported the spanwise distortion of streamwise velocity at different wall-normal locations, which is reproduced in figure 24(a). The dimensional variables U_A^* and z_A^* correspond to those of figure 1 in Asai & Nishioka (1989). For comparison, figure 24(b) presents our numerical results at the corresponding Reynolds number and the same streamwise and wall-normal positions, showing good agreement with the experimental data.

Antisymmetric distributions of the time-averaged streamwise velocity were reported by Nishioka *et al.* (1975) (reproduced in figure 25(a)) and by Asai & Nishioka (1989). These antisymmetries were also captured in our computations, as shown in figure 25(b). The spanwise locations for antisymmetric profiles were selected to exhibit the strongest antisymmetry.

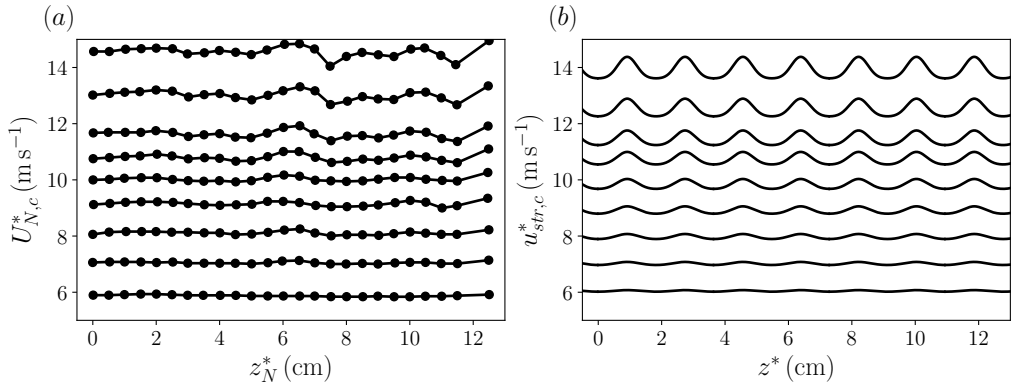


Figure 23: Comparison of streamwise velocity at the channel centreplane from experimental measurements and present numerical results at $x_h = 582$. Panel (a): experimental data from figure 2 of Nishioka *et al.* (1975). From bottom to top, $Re_c = 3000, 3500, 4000, 4500, 5000, 5500, 5900, 6500, 7300$. Panel (b): present numerical results computed with $\epsilon = 0.001$, $k_{x,h} = 0.005$, $k_{y,h} = \pi$, $k_{z,h} = 5\pi/2$ at the corresponding Re_h .

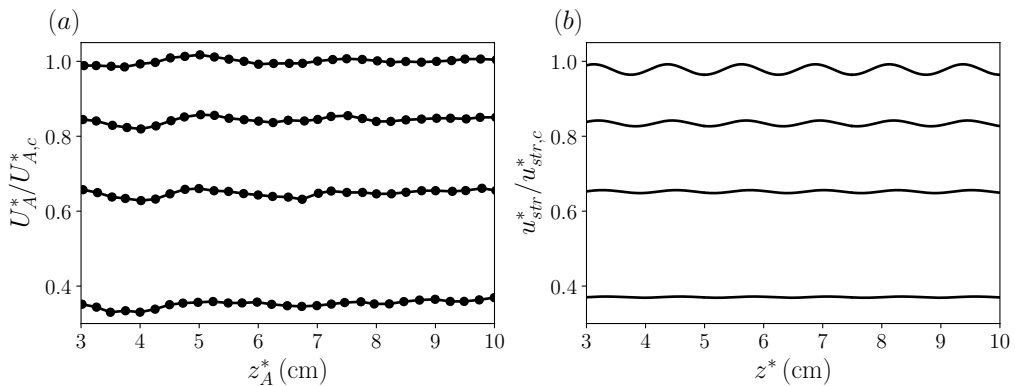


Figure 24: Comparison of streamwise velocity at different wall-normal locations from experimental measurements and present numerical results at $x_h = 637$. From bottom to top, $y_h = 0.2, 0.4, 0.59, 1$. Panel (a): experimental data from figure 1 of Asai & Nishioka (1989) at $Re_c = 5000$. Panel (b): present numerical results computed with $\epsilon = 0.0007$, $Re_h = 3333.3$, $k_{x,h} = 0.005$, $k_{y,h} = \pi$, $k_{z,h} = 0.59\pi$.

While Nishioka *et al.* (1975) attributed these distortions to warping of the upper wall, Asai & Nishioka (1989) ascribed them to non-uniformities in the damping screens or to the wall curvature in the contraction section, both of which may serve as sources of free-stream vortical disturbances. The comparison with our numerical results in figures 23–25 appear to support the first idea by Asai & Nishioka (1989), i.e. that the damping screens caused non-uniformities in the flow further downstream, because neither the warping of the walls nor the wall curvature is modelled in our study. Unfortunately, due to the absence of a detailed description of the free-stream vortical disturbances in the experiments, a more accurate comparison is not possible.

Figure 26 compares the experimental measurements of the streamwise velocity profiles of the forcing modes reported by Nishioka *et al.* (1975) (left) with those obtained in the present simulations (right). Due to symmetry about the channel centreplane, only the profiles for

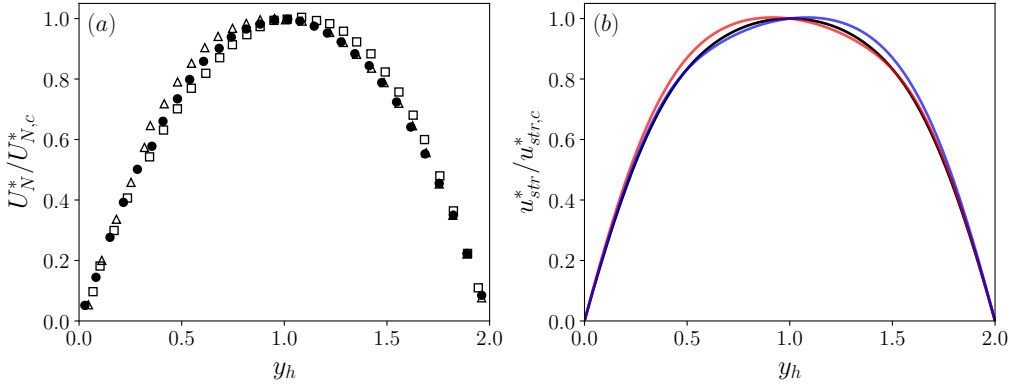


Figure 25: Comparison of streamwise velocity profiles from experimental measurements and present numerical results at $x_h = 582$ and different spanwise locations. Panel (a): experimental data from figure 3 of Nishioka *et al.* (1975) at $Re_c = 7500$ and spanwise locations z_N^* (cm) = 3 (squares), 6 (triangles), 9 (circles). Panel (b): present numerical results at $\bar{z} = 5\pi/16$ (red), $\pi/2$ (black) and $11\pi/16$ (blue) computed with $\epsilon = 0.002$, $Re_h = 5000$, $k_{x,h} = 0.005$, $k_{y,h} = \pi$, $k_{z,h} = 5\pi/2$.

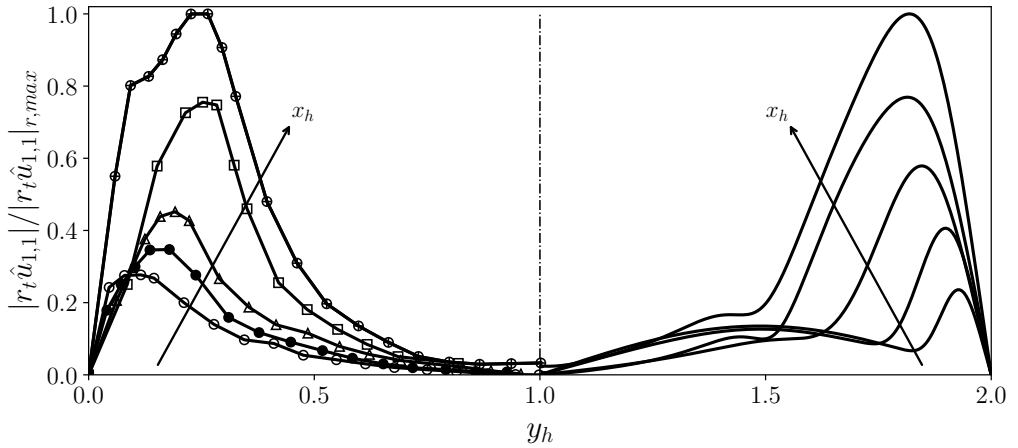


Figure 26: Comparison of streamwise velocity profiles of the fundamental fluctuation from experimental measurements and present numerical results at $Re_c = 5000$. Left: experimental data from figure 18 of Nishioka *et al.* (1975). Right: present numerical results computed with $\epsilon = 0.005$, $Re_h = 3333.3$, $k_{x,h} = 0.005$, $k_{y,h} = \pi$, $k_{z,h} = \pi$. The velocity is normalised by $|r_t \hat{u}_{1,1}|_{r,max}$, the maximum value of the reference profile, corresponding here to the most downstream profile.

a half channel are shown. The comparison is qualitative because their perturbations were generated far from the channel mouth. In both cases, the profiles close to the source exhibit their maximum near the wall, at a distance of approximately 0.1. As the perturbation grows algebraically, the effect of nonlinearity is analogous, i.e. the peak initially moves toward the centreplane, while, farther downstream, its distance from the wall remains almost constant and smaller than a quarter of the channel height.

4. Summary and conclusions

As a step towards understanding laminar–turbulent transition in channel flow, we have investigated the nonlinear evolution of free-stream vortical disturbances entrained in the entrance region of a channel using high Reynolds number asymptotic and numerical methods. The perturbation flow along the channel entrance is triggered by symmetric and antisymmetric disturbances at the channel mouth, modelled as low-frequency vortical modes of the convected gust type.

The effects of the Reynolds number, the amplitude and the streamwise, wall-normal and spanwise wavelengths of the inlet disturbances on the nonlinear flow evolution have been investigated parametrically. A significant amplification of perturbation intensity is observed at the channel inlet for the symmetric case, while, in the antisymmetric case, the perturbation amplitude grows mildly from the channel mouth, then decays and eventually intensifies downstream. Farther downstream, the perturbation decays in both cases when weak or moderate inlet disturbances are imposed, although its amplitude remains considerable even when the base flow is fully developed. For flows triggered by strong antisymmetric inlet disturbances, the perturbation amplitude eventually saturates downstream. This behaviour is different from the nonlinear disturbance evolution in circular pipes, which instead decay by viscous effects following their initial growth (Zhu & Ricco 2024). Nonlinearity is found to play a stabilising effect on the intense algebraic growth, i.e. the linear theory overpredicts the amplitude. The distortion of the laminar base flow given by nonlinearity grows significantly, causing an increase in wall-shear stress.

The disturbances evolve into streamwise elongated channel-entrance nonlinear structures (ECENS), featuring low-speed and high-speed regions meandering in the streamwise direction. Instead of being confined to the near-wall region as in the cases of open boundary layers exposed to free-stream turbulence, the ECENS occupy the entire channel cross section. The ECENS generated by symmetric and antisymmetric inlet disturbances are distinctly different. At sufficiently large inlet amplitudes, the downstream character however becomes less dependent on the inlet symmetry. The ECENS are characterised in these cases by streamwise vortices flanked by two low-speed regions and two high-speed regions. They possess a half-turn rotational symmetry with respect to the vortex centres. Using three well-defined criteria, the presence of travelling waves is identified. They span both the developing region and the fully developed region. Their phase speed is more than double the bulk velocity.

The similarities and differences between the ECENS and the nonlinear structures discovered by Wall & Nagata (2016) in the fully developed region are discussed. The experimental studies of Nishioka and coworkers (Nishioka *et al.* 1975; Asai & Nishioka 1989) focused on the stability and transition of channel flow caused by disturbances induced by a vibrating ribbon located in the fully developed region. Results obtained without artificial excitation, where the flow was subject only to free-stream disturbances originating from the damping screen and/or the contraction section, were also reported and have been used for comparison with our numerical results. Good agreement is observed between their results and ours, both of which exhibit spanwise distortions of the streamwise velocity profiles. Our results also show excellent agreement with the theoretical predictions by Sadri & Floryan (2002) and with the experimental measurements by Asai & Floryan (2004) in the downstream region of the flow.

The inclusion of a continuous spectrum of inlet disturbances, the secondary instability analysis of the nonlinear ECENS and DNS of the fully-fledged transition are further research steps towards more realistic and industrially relevant applications. The secondary-stability framework of Herbert (1983*b*), applied to nonlinear two-dimensional neutral travelling waves,

could be extended to the three-dimensional travelling waves discovered in our study. Further ideas on the subsequent development of secondary-instability modes are found in Herbert (1988). We also propose the use of ECENS as initial guesses for the search of new families of exact coherent structures (ECS) in fully developed channel flow. While most ECS identified in fully developed pipe and channel flows exhibit a characteristic streamwise length scale comparable to the pipe diameter or the channel height, DNS performed in long computational domains have shown the existence of streamwise-localised ECS with an elongated streamwise length scale (refer to Mellibovsky *et al.* (2009), Avila *et al.* (2013) and Chantry *et al.* (2014) for pipe flow, and Zammert & Eckhardt (2014, 2016) for channel flow). Given the richness of the phase space and our computations of ECENS, we therefore anticipate that additional streamwise-elongated ECS may exist in fully developed channel flow when sufficiently long computational domains are considered. We further advocate for research activity on the physical mechanisms behind the difference between channel and pipe flows, focusing on the reasons why the perturbations persist in the channel-flow geometry. We hope that the results presented here will inspire further DNS and experimental investigations in the entrance region of confined flows.

Acknowledgements. The authors would like to thank the Faculty of Engineering at the University of Sheffield for funding this research. We are also indebted to Dr Elena Marensi, Dr Bo Yuan and Prof. Rich Kerswell for the inspiring conversations and suggestions. We acknowledge the referees' comments, which have helped improve the quality of our paper.

Funding. This work was funded by the Faculty of Engineering University Research Scholarship from the University of Sheffield.

Declaration of interests. The authors report no conflict of interest.

Appendix A. Mathematical formulation for the development of steady perturbations

In §2, the streamwise wavenumber k_x is used to scale the variables t and x and therefore the steady case cannot be studied by that formulation. To study the dynamics of steady perturbations in channel flow, we introduce the slow variables $\check{t} = Re_\lambda^{-1}t$ and $\check{x} = Re_\lambda^{-1}x$, and decompose the velocity and pressure as follows:

$$\begin{aligned} \{\mathbf{u}, p\} &= \{U, P\} + \{\check{\mathbf{u}}, \check{p}\} \\ &= \begin{pmatrix} U(\check{x}, y) \\ Re_\lambda^{-1}V(\check{x}, y) \\ 0 \\ P(\check{x}) \end{pmatrix} + r_t \sum_{m,n=-\infty}^{\infty} \begin{pmatrix} \check{u}_{m,n} \\ Re_\lambda^{-1}\check{v}_{m,n} \\ Re_\lambda^{-1}\check{w}_{m,n} \\ \check{\Gamma}_{m,n} + Re_\lambda^{-2}\check{p}_{m,n} \end{pmatrix} e^{im\check{k}_x\check{t} + ink_z z}, \end{aligned} \quad (\text{A } 1)$$

where $\check{k}_x = k_x Re_\lambda$. As in the scaling adopted in §2, the boundary-layer equations governing the laminar base flow and the steady nonlinear boundary-region equations governing the perturbation flow are obtained by substituting (A 1) into the Navier-Stokes equations (2.4)–(2.5) and taking the limits $\check{k}_x \rightarrow 0$, $Re_\lambda \rightarrow \infty$. The laminar boundary-layer equations read

$$\frac{\partial U}{\partial \check{x}} + \frac{\partial V}{\partial y} = 0, \quad (\text{A } 2)$$

$$U \frac{\partial U}{\partial \check{x}} + V \frac{\partial U}{\partial y} = -\frac{dP}{d\check{x}} + \frac{\partial^2 U}{\partial y^2}. \quad (\text{A } 3)$$

The steady nonlinear boundary-region equations read

$$\frac{\partial \check{u}_{m,n}}{\partial \check{x}} + \frac{\partial \check{v}_{m,n}}{\partial y} + ink_z \check{w}_{m,n} = 0, \quad (\text{A } 4)$$

$$\left(\frac{\partial U}{\partial \check{x}} + n^2 k_z^2 \right) \check{u}_{m,n} + U \frac{\partial \check{u}_{m,n}}{\partial \check{x}} + V \frac{\partial \check{u}_{m,n}}{\partial y} + \check{v}_{m,n} \frac{\partial U}{\partial y} - \frac{\partial^2 \check{u}_{m,n}}{\partial y^2} + \frac{d\check{\Gamma}_{m,n}}{d\check{x}} = r_t \check{\mathcal{X}}_{m,n}, \quad (\text{A } 5)$$

$$\left(\frac{\partial V}{\partial y} + n^2 k_z^2 \right) \check{v}_{m,n} + U \frac{\partial \check{v}_{m,n}}{\partial \check{x}} + \check{u}_{m,n} \frac{\partial V}{\partial \check{x}} + V \frac{\partial \check{v}_{m,n}}{\partial y} + \frac{\partial \check{p}_{m,n}}{\partial y} - \frac{\partial^2 \check{v}_{m,n}}{\partial y^2} = r_t \check{\mathcal{Y}}_{m,n}, \quad (\text{A } 6)$$

$$n^2 k_z^2 \check{w}_{m,n} + U \frac{\partial \check{w}_{m,n}}{\partial \check{x}} + V \frac{\partial \check{w}_{m,n}}{\partial y} + ink_z \check{p}_{m,n} - \frac{\partial^2 \check{w}_{m,n}}{\partial y^2} = r_t \check{\mathcal{Z}}_{m,n}, \quad (\text{A } 7)$$

where $\check{\mathcal{X}}_{m,n}$, $\check{\mathcal{Y}}_{m,n}$, and $\check{\mathcal{Z}}_{m,n}$ have the same form as those in (2.19), but are expressed using the steady-state notation (A 1). Equations (A 4)–(A 7) can also be obtained from (2.15)–(2.18) by neglecting the terms arising from time derivatives and setting $\mathcal{F} = 1$.

Appendix B. Conservation of the mass flow rate

At each instant in time and at each streamwise location, the mass flow rate is conserved. Since the flow is incompressible, this condition translates to the conservation of the bulk velocity, i.e. the streamwise velocity averaged on the cross section of the channel is equal to the oncoming velocity U_∞^* ,

$$\frac{1}{2h\lambda_z} \int_{-\lambda_z/2}^{\lambda_z/2} \int_0^{2h} (U + r_t \bar{u}) dy dz = 1. \quad (\text{B } 1)$$

We thus obtain equation (2.11) for the laminar base flow, and

$$\sum_{m,n=-\infty}^{\infty} \int_{-\lambda_z/2}^{\lambda_z/2} \int_0^{2h} \left(\hat{u}_{m,n} e^{im\bar{t} + ink_z z} \right) dy dz = 0, \quad (\text{B } 2)$$

for perturbation flow by substituting (2.7) into (B 1). By using the orthogonality property of the Fourier series, equation (2.20) is obtained. This condition is needed to solve the system because the pressure $\hat{\Gamma}_{m,0}$ is an additional unknown.

Appendix C. Initial conditions: velocity contours and comparison with previous studies

Figure 27 shows the contours of the velocity components \tilde{u} , \tilde{v} and \tilde{w} of the initial conditions induced by the antisymmetric free-stream disturbance (defined in (2.1) with $\hat{u}_{y_\pm}^\infty = \pm 1$, $\hat{v}_{y_\pm}^\infty = -1$ and $\hat{w}_{y_\pm}^\infty = \pm 1$) near the channel inlet ($x_h = 0.225$). Four time instants, $\bar{t} = 0, \pi/4, \pi/2, 3\pi/4$, are shown to highlight the time evolution. The initial conditions are composite solutions derived by Ricco & Alvarenga (2021) using matched asymptotic expansions, combining an inviscid outer solution that matches the upstream free-stream disturbance with a viscous inner solution resulting from the channel confinement. These composite solutions are illustrated in the core and the near-wall regions in figure 27. As the amplitudes of the three velocity components vary with time, their peak values remain of order $O(10^{-2})$. The antisymmetry of the streamwise and spanwise velocity components and the symmetry of the wall-normal velocity component are slightly altered due to the effect of confinement.

The contours of the velocity components \tilde{u} , \tilde{v} and \tilde{w} of the initial conditions induced by

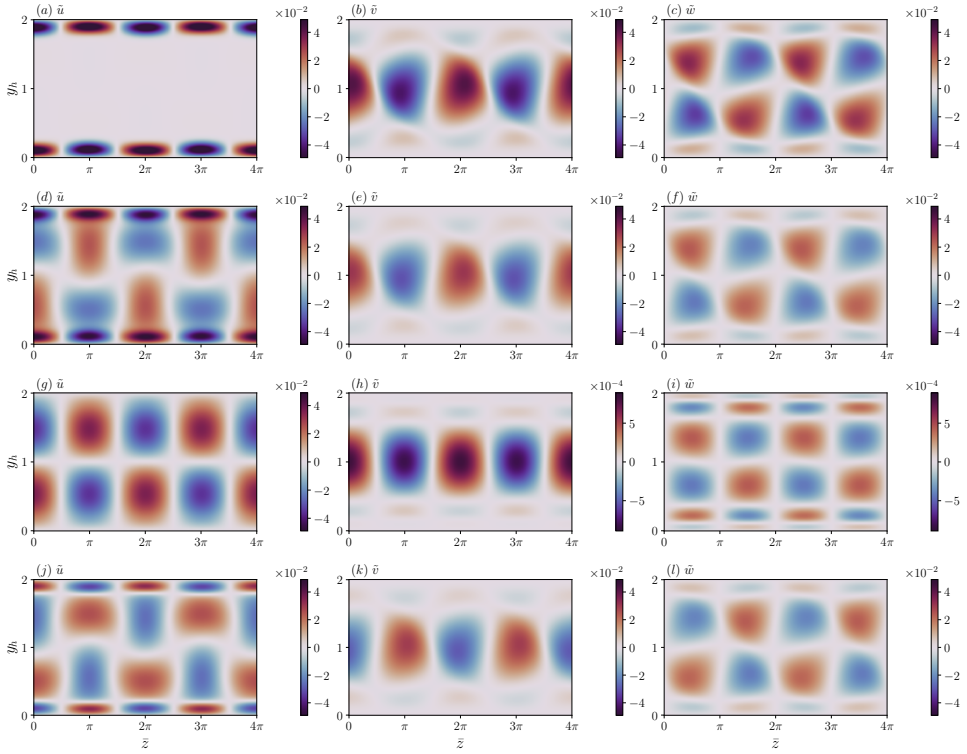


Figure 27: Contours of the velocity components \tilde{u} , \tilde{v} and \tilde{w} (from left to right) of the initial conditions induced by the antisymmetric free-stream disturbance at $x_h = 0.225$, for $\tilde{t} = 0, \pi/4, \pi/2, 3\pi/4$ (from top to bottom). The colourbar scaling in (h) and (i) differs from the others.

the symmetric free-stream disturbance (defined in (2.1) with $\hat{u}_{y_{\pm}}^{\infty} = 1$, $\hat{v}_{y_{\pm}}^{\infty} = \mp 1$ and $\hat{w}_{y_{\pm}}^{\infty} = 1$) are shown in figure 28. As in the antisymmetric case, the maximum amplitudes of the three velocity components are comparable and the symmetry of the free-stream disturbance is mildly altered.

Our initial condition differs from that used by Duck (2005) for a few reasons. Duck (2005) employed an eigenfunction, found by Luchini (1996), that satisfies the three-dimensional boundary-layer equations. It is steady and its evolution is unaffected at leading order by spanwise viscous effects because the spanwise wavelength of the disturbance is much larger than the boundary-layer thickness. Furthermore, the streamwise and spanwise velocity components vanish in the channel core. The wall-normal velocity component tends to a constant value in the open boundary layer case, while, in Duck (2005)'s case, it vanishes to zero at the centreplane through an induced inviscid potential. The main difference from our initial condition is that this eigenfunction grows downstream as $(x^*/L^*)^{0.213}$, where L^* is the distance from the leading edge, while ours grows linearly downstream in the boundary-layer limit because it is forced by the convected gusts existing in the channel core (Crow 1966; Leib *et al.* 1999). The main difference between our initial conditions and those used by Buffat *et al.* (2014) and Alizard *et al.* (2018) in their DNS studies is that they employed steady optimal disturbances that were confined within the developing boundary layers and vanished in the channel core. The location of the initial perturbation was also different, i.e. $x^*/h^* = 4$ in Buffat *et al.* (2014) and $x^*/h^* = 16$ in Alizard *et al.* (2018).

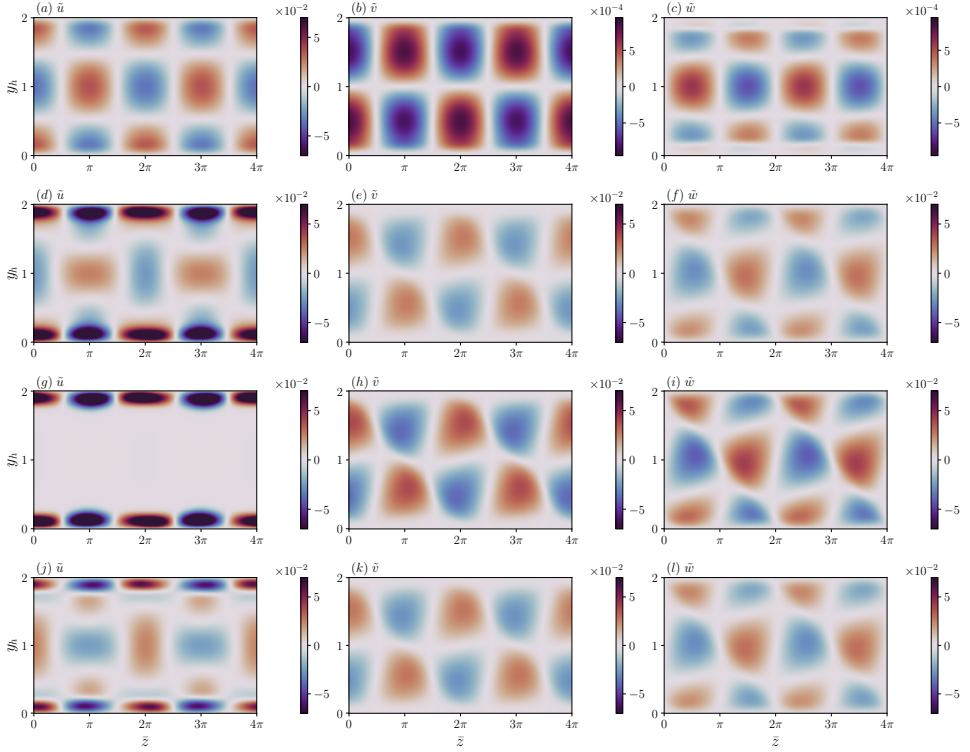


Figure 28: Contours of the velocity components \tilde{u} , \tilde{v} and \tilde{w} (from left to right) of the initial conditions induced by the symmetric free-stream disturbance at $x_h = 0.225$, for $\tilde{t} = 0, \pi/4, \pi/2, 3\pi/4$ (from top to bottom). The colourbar scaling in (b) and (c) differs from the others.

Appendix D. Coefficients of equation (2.27)

The expressions of \mathcal{V} , \mathcal{V}_y , \mathcal{V}_x , \dots , \mathcal{U}_{xy} in equation (2.27) are

$$\mathcal{V} = imn^2k_z^2 + n^2k_z^2\frac{\partial V}{\partial y} + \frac{n^4k_z^4}{\mathcal{F}} - \frac{\partial^3 V}{\partial y^3},$$

$$\mathcal{V}_y = n^2k_z^2V - \frac{\partial^2 V}{\partial y^2},$$

$$\mathcal{V}_x = n^2k_z^2U + \frac{\partial^2 U}{\partial y^2},$$

$$\mathcal{V}_{yy} = -\left(im + \frac{2n^2k_z^2}{\mathcal{F}} + \frac{\partial V}{\partial y}\right),$$

$$\mathcal{V}_{yyy} = -V,$$

$$\mathcal{V}_{xyy} = -U,$$

$$\mathcal{V}_{yyyy} = \frac{1}{\mathcal{F}},$$

$$\mathcal{U} = n^2k_z^2\frac{\partial V}{\partial \bar{x}} - \frac{\partial^3 V}{\partial \bar{x}\partial y^2},$$

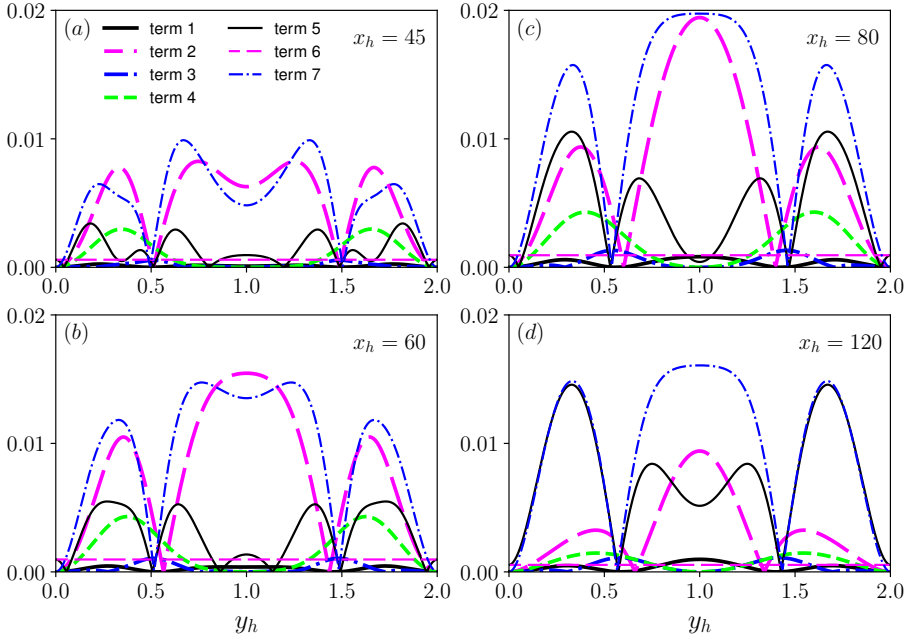


Figure 29: Amplitudes of the terms of the x -momentum equation (2.16) for mode $(0, 0)$ as a function of y_h at different x_h locations. Legends are the same for figure 30.

$$\mathcal{U}_x = 2 \frac{\partial^2 U}{\partial \bar{x} \partial y},$$

$$\mathcal{U}_{yy} = \frac{\partial V}{\partial \bar{x}},$$

$$\mathcal{U}_{xy} = 2 \frac{\partial U}{\partial \bar{x}}.$$

Appendix E. Dynamics of the most energetic modes

The dynamics of modes $(0, 0)$ and $(1, 1)$ is studied by analysing the terms of the x -momentum equation (2.16). The modes are the most energetic during the disturbance growth in the antisymmetric case. Figure 29 shows that the dynamics of the mean-flow distortion, i.e. mode $(0, 0)$, is dominated by the balance between the linear convection term 2 ($U \partial \hat{u}_{0,0} / \partial \bar{x}$) and the nonlinear term 7 ($r_t \mathcal{X}_{0,0}$) up to $x_h = 80$. Further downstream, i.e. for $x_h > 80$, the linear convection term 2 decreases in amplitude and nonlinearity is instead balanced almost entirely by the viscous term 5 ($\mathcal{F}^{-1} \partial^2 \hat{u}_{0,0} / \partial y^2$) near the wall. Figure 30 shows that the balance of terms for mode $(1, 1)$ is distinctly different as the lift-up term 4 ($\hat{v}_{1,1} \partial U / \partial y$) governs the dynamics at all x_h . This term is balanced inviscidly by the linear convection term 2 ($U \partial \hat{u}_{1,1} / \partial \bar{x}$) up to $x_h = 60$, while further downstream ($x_h = 120$) it is mostly balanced by the nonlinear term ($r_t \mathcal{X}_{1,1}$).

REFERENCES

DEL ÁLAMO, J. C. & JIMÉNEZ, J. 2006 Linear energy amplification in turbulent channels. *J. Fluid Mech.* **559**, 205–213.

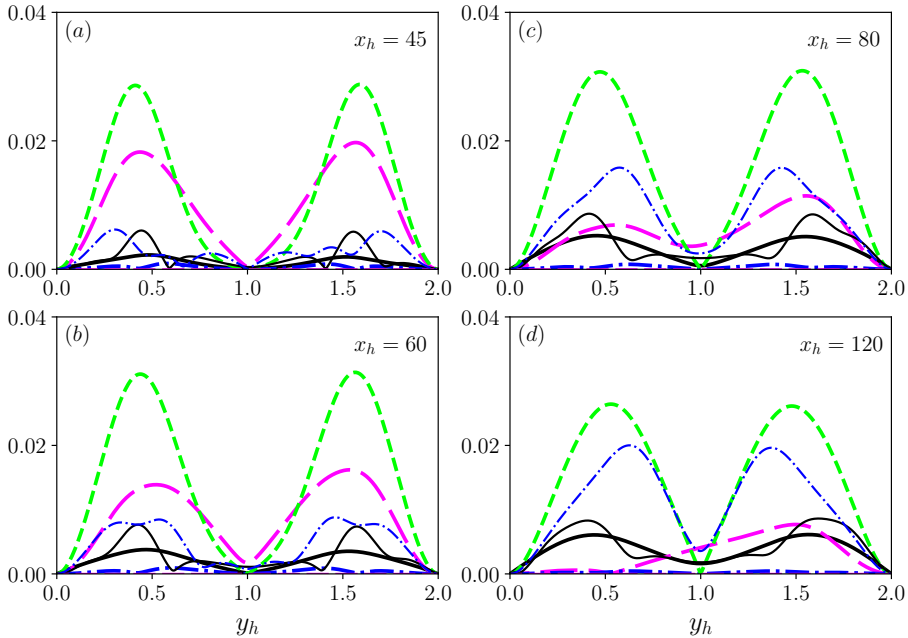


Figure 30: Amplitudes of the terms of the x -momentum equation (2.16) for mode (1, 1) as a function of y_h at different x_h locations.

- ALIZARD, F., CADIOU, A., LE PENVEN, L., DI PIERRO, B. & BUFFAT, M. 2018 Space-time dynamics of optimal wavepackets for streaks in a channel entrance flow. *J. Fluid Mech.* **844**, 669–706.
- ASAI, M. & FLORYAN, J.M. 2004 Certain aspects of channel entrance flow. *Phys. Fluids* **16** (4), 1160–1163.
- ASAI, M. & NISHIOKA, M. 1989 Origin of the peak-valley wave structure leading to wall turbulence. *J. Fluid Mech.* **208**, 1–23.
- AVILA, M., MELLIBOVSKY, F., ROLAND, N. & HOF, B. 2013 Streamwise-Localized Solutions at the Onset of Turbulence in Pipe Flow. *Phys. Rev. Lett.* **110** (22), 224502.
- BIAU, D. 2008 Linear stability of channel entrance flow. *Eur. J. Mech. B/Fluids* **27** (5), 579–590.
- BODOIA, J. R. & OSTERLE, J. F. 1961 Finite difference analysis of plane Poiseuille and Couette flow developments. *Appl. Sci. Res.* **10**, 265–276.
- BORODULIN, V. I., IVANOV, A. V., KACHANOV, Y. S. & ROSCHEKTAYEV, A. P. 2021 Distributed vortex receptivity of a swept-wing boundary layer. Part 1. Efficient excitation of CF modes. *J. Fluid Mech.* **908**, A14.
- BUFFAT, M., LE PENVEN, L., CADIOU, A. & MONTAGNIER, J. 2014 DNS of bypass transition in entrance channel flow induced by boundary layer interaction. *Eur. J. Mech. B/Fluids* **43**, 1–13.
- BUTLER, K. M. & FARRELL, B. F. 1992 Three-dimensional optimal perturbations in viscous shear flow. *Phys. Fluids* **4** (8), 1637–1650.
- BUTLER, K. M. & FARRELL, B. F. 1993 Optimal perturbations and streak spacing in wall-bounded turbulent shear flow. *Phys. Fluids* **5** (3), 774–777.
- CARLSON, D. R., WIDNALL, S. E. & PEETERS, M. F. 1982 A flow-visualization study of transition in plane Poiseuille flow. *J. Fluid Mech.* **121**, 487–505.
- CEBECI, T. 2002 *Convective heat transfer*. Springer.
- CHANTRY, M., WILLIS, A. P. & KERSWELL, R. R. 2014 Genesis of streamwise-localized solutions from globally periodic traveling waves in pipe flow. *Phys. Rev. Lett.* **112** (16), 23–27.
- CHEN, T. S. & SPARROW, E. M. 1967 Stability of the developing laminar flow in a parallel-plate channel. *J. Fluid Mech.* **30** (2), 209–224.
- CROW, S.C. 1966 The spanwise perturbation of two-dimensional boundary-layers. *J. Fluid Mech.* **24**, 153–164.

- DAVIES, S. J. & WHITE, C. M. 1928 An experimental study of the flow of water in pipes of rectangular section. *Proc. R. Soc. Lond. A* **119** (781), 92–107.
- DEGUCHI, K., HALL, P. & WALTON, A. 2013 The emergence of localized vortex–wave interaction states in plane Couette flow. *J. Fluid Mech.* **721**, 58–85.
- DIETZ, A. J. 1999 Local boundary-layer receptivity to a convected free-stream disturbance. *J. Fluid Mech.* **378**, 291–317.
- DRAZIN, P. G. & REID, W. H. 2004 *Hydrodynamic Stability*, 2nd edn. Cambridge: Cambridge University Press.
- DUCK, P. W. 2005 Transient growth in developing plane and Hagen Poiseuille flow. *Proc. R. Soc. A* **461** (2057), 1311–1333.
- DURST, F., RAY, S., ÜNSAL, B. & BAYOUMI, O. A. 2005 The development lengths of laminar pipe and channel flows. *J. Fluids Eng.* **127** (6), 1154–1160.
- ENGEL, M., ASHTARI, O., SCHNEIDER, T. M. & LINKMANN, M. 2025 Search for unstable relative periodic orbits in channel flow using symmetry-reduced dynamic mode decomposition. *J. Fluid Mech.* **1013**, A45.
- FANG, Z. & SABER, A. J. 1987 Marching control volume finite-element calculation for developing entrance flow. *AIAA journal* **25** (2), 346–348.
- GARG, V.K. & GUPTA, S.C. 1981*a* Stability of the nonparallel developing flow in a channel. *Comput. Meth. Appl. Mech. Engng* **29** (3), 259–269.
- GARG, V. K. & GUPTA, S. C. 1981*b* Nonparallel effects on the stability of developing flow in a channel. *Phys. Fluids* **24** (9), 1752–1754.
- GIBSON, J. F. & BRAND, E. 2014 Spanwise-localized solutions of planar shear flows. *J. Fluid Mech.* **745**, 25–61.
- GRAHAM, M. D & FLORYAN, D. 2021 Exact coherent states and the nonlinear dynamics of wall-bounded turbulent flows. *Annu. Rev. Fluid Mech.* **53** (1), 227–253.
- GROSCH, C. E. & SALWEN, H. 1968 The stability of steady and time-dependent plane Poiseuille flow. *J. Fluid Mech.* **34** (1), 177–205.
- GUPTA, S. C. & GARG, V. K. 1981*a* Effects of velocity distribution on the stability of developing flow in a channel. *J. Phys. Soc. Jpn.* **50** (2), 673–680.
- GUPTA, S. C. & GARG, V. K. 1981*b* Linear spatial stability of developing flow in a parallel plate channel. *J. Appl. Mech.* **48**.
- GUPTA, S. C. & GARG, V. K. 1981*c* Stability of developing flow in a two-dimensional channel—Symmetric vs. antisymmetric disturbances. *Comput. Meth. Appl. Mech. Engng* **27** (3), 363–368.
- GUSTAVSSON, L. H. 1991 Energy growth of three-dimensional disturbances in plane Poiseuille flow. *J. Fluid Mech.* **224**, 241–260.
- HAHNEMANN, E., FREEMAN, J. C. & FINSTON, M. 1948 Stability of boundary layers and of flow in entrance section of a channel. *J. Aerosp. Sci.* **15** (8), 493–496.
- HALL, P. 1983 The linear development of Görtler vortices in growing boundary layers. *J. Fluid Mech.* **130**, 41–58.
- HALL, P. 1988 The nonlinear development of Görtler vortices in growing boundary layers. *J. Fluid Mech.* **193**, 243–266.
- HALL, P. & SMITH, F. T. 1991 On strongly nonlinear vortex/wave interactions in boundary-layer transition. *J. Fluid Mech.* **227**, 641–666.
- HAMEL, G. 1917 Spiralförmige bewegungen zäher flüssigkeiten. *Jahresber. Dtsch. Math.-Ver.* **25**, 34–60.
- HAMILTON, J. M., KIM, J. & WALEFFE, F. 1995 Regeneration mechanisms of near-wall turbulence structures. *J. Fluid Mech.* **287**, 317–348.
- HEISENBERG, W. 1924 Über stabilität und turbulenz von flüssigkeitsströmen. *Ann. Phys.* **4** (74), 577–627.
- HERBERT, T. 1980 Nonlinear stability of parallel flows by high-ordered amplitude expansions. *AIAA J.* **18** (3), 243–248.
- HERBERT, T. 1983*a* On perturbation methods in nonlinear stability theory. *J. Fluid Mech.* **126**, 167–186.
- HERBERT, T. 1983*b* Secondary instability of plane channel flow to subharmonic three-dimensional disturbances. *Phys. Fluids* **26** (4), 871–874.
- HERBERT, T. 1984*a* Nonlinear effects in hydrodynamic stability. *Special Course On Stability and Transition of Laminar Flow (Agard-R-709)(Agard, Neuilly-sur-Seine, France)* .
- HERBERT, T. 1984*b* Secondary instability of shear flows. *Special Course On Stability and Transition of Laminar Flow (Agard-R-709)(Agard, Neuilly-sur-Seine, France)* .

- HERBERT, T. 1988 Secondary instability of boundary layers. *Ann. Rev. Fluid Mech.* **20**, 487–526.
- HOF, B., VAN DOORNE, C.W.H., WESTERWEEL, J., NIEUWSTADT, F.T.M., FAISST, H., ECKHARDT, B., WEDIN, H., KERSWELL, R.R. & WALEFFE, F. 2004 Experimental observation of nonlinear traveling waves in turbulent pipe flow. *Science* **305** (5690), 1594–1598.
- JEFFERY, G.B. 1915 The two-dimensional steady motion of a viscous fluid. *Philos. Mag.* **29** (172), 455–465.
- KAO, T. W. & PARK, C. 1970 Experimental investigations of the stability of channel flows. Part 1. Flow of a single liquid in a rectangular channel. *J. Fluid Mech.* **43** (1), 145–164.
- KEMP, N. 1951 The laminar three-dimensional boundary layer and a study of the flow past a side edge. Msc thesis, Cornell University, Ithaca, NY.
- KIM, J, MOIN, P & MOSER, R 1987 Turbulence statistics in fully developed channel flow at low Reynolds number. *J. Fluid Mech.* **177**, 133–166.
- LEIB, S.J., WUNDROW, D.W. & GOLDSTEIN, M.E. 1999 Effect of free-stream turbulence and other vortical disturbances on a laminar boundary layer. *J. Fluid Mech.* **380**, 169–203.
- LIN, C. C. 1946 On the stability of two-dimensional parallel flows. III. Stability in a viscous fluid. *Quart. Appl. Math.* **3** (4), 277–301.
- LUCHINI, P. 1996 Reynolds-number-independent instability of the boundary layer over a flat surface. *J. Fluid Mech.* **327**, 101–115.
- MARENSI, E. & RICCO, P. 2017 Growth and wall-transpiration control of nonlinear unsteady Görtler vortices forced by free-stream vortical disturbances. *Phys. Fluids* **29** (11), 114106.
- MARENSI, E., RICCO, P. & WU, X. 2017 Nonlinear unsteady streaks engendered by the interaction of free-stream vorticity with a compressible boundary layer. *J. Fluid Mech.* **817**, 80–121.
- MATSUBARA, M. & ALFREDSSON, P.H. 2001 Disturbance growth in boundary layers subjected to free-stream turbulence. *J. Fluid Mech.* **430**, 149–168.
- MELIBOVSKY, F., MESEGUER, A., SCHNEIDER, T. M. & ECKHARDT, B. 2009 Transition in localized pipe flow turbulence. *Phys. Rev. Lett.* **103** (5), 054502.
- NAGATA, M. & DEGUCHI, K. 2013 Mirror-symmetric exact coherent states in plane Poiseuille flow. *J. Fluid Mech.* **735**, R4.
- NISHIOKA, M., IID A, S. & ICHIKAWA, Y. 1975 An experimental investigation of the stability of plane Poiseuille flow. *J. Fluid Mech.* **72** (4), 731–751.
- NISHIOKA, T., HONDA, S. & KAMIBAYASHI, S. 1981 An experimental investigation on the subcritical instability in plane Poiseuille flow. Technical Report TM-75885. NASA, Washington, DC.
- ORSZAG, S. A. 1971 Accurate solution of the Orr–Sommerfeld stability equation. *J. Fluid Mech.* **50** (4), 689–703.
- PATEL, V. C. & HEAD, M. R. 1969 Some observations on skin friction and velocity profiles in fully developed pipe and channel flows. *J. Fluid Mech.* **38** (1), 181–201.
- PFENNIGER, W 1961 Transition in the inlet length of tubes at high Reynolds numbers. *Boundary layer and flow control* pp. 970–980.
- POPE, S.B. 2000 *Turbulent flows*. Cambridge University Press.
- PUGH, J.D. 1988 Finite amplitude waves in plane Poiseuille flow. PhD thesis, California Institute of Technology.
- PUJALS, G., GARCÍA-VILLALBA, M., COSSU, C. & DEPARDON, S. 2009 A note on optimal transient growth in turbulent channel flows. *Phys. Fluids* **21** (1), 015109.
- RAVI SANKAR, S., NANDAKUMAR, K. & MASLIYAH, J. H. 1988 Oscillatory flows in coiled square ducts. *The Physics of Fluids* **31** (6), 1348–1359.
- REDDY, S. C. & HENNINGSON, D. S. 1993 Energy growth in viscous channel flows. *J. Fluid Mech.* **252**, 209–238.
- REYNOLDS, O. 1883 XXIX. An experimental investigation of the circumstances which determine whether the motion of water shall be direct or sinuous, and of the law of resistance in parallel channels. *Phil. Trans. R. Soc.* (174), 935–982.
- RICCO, P. & ALVARENGA, C. 2021 Entrainment and growth of vortical disturbances in the channel-entrance region. *J. Fluid Mech.* **927**, A18.
- RICCO, P. & ALVARENGA, C. 2022 Growth of vortical disturbances entrained in the entrance region of a circular pipe. *J. Fluid Mech.* **932**, A16.
- RICCO, P., LUO, J. & WU, X. 2011 Evolution and instability of unsteady nonlinear streaks generated by free-stream vortical disturbances. *J. Fluid Mech.* **677**, 1–38.
- RICCO, P. & WU, X. 2007 Response of a compressible laminar boundary layer to free-stream vortical disturbances. *J. Fluid Mech.* **587**, 97–138.

- SADRI, R.M. & FLORYAN, J.M. 2002 Entry flow in a channel. *Comput. Fluids* **31** (2), 133–157.
- SCHMID, P. J. & HENNINGSON, D. S. 2001 *Stability and transition in shear flows*. Springer.
- SHEKAR, A. & GRAHAM, M. D. 2018 Exact coherent states with hairpin-like vortex structure in channel flow. *J. Fluid Mech.* **849**, 76–89.
- SHEN, S. F. 1954 Calculated amplified oscillations in the plane Poiseuille and Blasius flows. *J. Aero. Sci.* **21** (1), 62–64.
- SONG, R. & DEGUCHI, K. 2025 Three-dimensional coherent structures in a curved pipe flow. *J. Fluid Mech.* **1007**, A34.
- SPARROW, E. M., LIN, S. H. & LUNDGREN, T. S. 1964 Flow development in the hydrodynamic entrance region of tubes and ducts. *Phys. Fluids* **7** (3), 338–347.
- STUART, J. T. 1963 *Hydrodynamic stability*. New York: Oxford University Press.
- THOMAS, L. H. 1953 The stability of plane Poiseuille flow. *Phys. Rev.* **91**, 780–783.
- TOH, S. & ITANO, T. 2003 A periodic-like solution in channel flow. *J. Fluid Mech.* **481**, 67–76.
- VAN DYKE, M. 1970 Entry flow in a channel. *J. Fluid Mech.* **44** (4), 813–823.
- WALEFFE, F. 1997 On a self-sustaining process in shear flows. *Phys. Fluids* **9** (4), 883–900.
- WALEFFE, F. 1998 Three-dimensional coherent states in plane shear flows. *Phys. Rev. Lett.* **81**, 4140–4143.
- WALEFFE, F. 2001 Exact coherent structures in channel flow. *J. Fluid Mech.* **435**, 93–102.
- WALEFFE, F. 2003 Homotopy of exact coherent structures in plane shear flows. *Phys. Fluids* **15** (6), 1517–1534.
- WALL, D. P. & NAGATA, M. 2016 Exact coherent states in channel flow. *J. Fluid Mech.* **788**, 444–468.
- WEDIN, H. & KERSWELL, R.R. 2004 Exact coherent structures in pipe flow: travelling wave solutions. *J. Fluid Mech.* **508**, 333–371.
- WU, X., ZHAO, D. & LUO, J. 2011 Excitation of steady and unsteady Görtler vortices by free-stream vortical disturbances. *J. Fluid Mech.* **682**, 66–100.
- XU, D., RICCO, P. & MARENSI, E. 2024 Excitation and stability of nonlinear compressible Görtler vortices and streaks induced by free-stream vortical disturbances. *J. Fluid Mech.* **1000**, A93.
- XU, D., ZHANG, Y. & WU, X. 2017 Nonlinear evolution and secondary instability of steady and unsteady Görtler vortices induced by free-stream vortical disturbances. *J. Fluid Mech.* **829**, 681–730.
- YANG, Q., WILLIS, A. P. & HWANG, Y. 2019 Exact coherent states of attached eddies in channel flow. *J. Fluid Mech.* **862**, 1029–1059.
- ZAMMERT, S. & ECKHARDT, B. 2014 Streamwise and doubly-localised periodic orbits in plane Poiseuille flow. *J. Fluid Mech.* **761**, 348–359.
- ZAMMERT, S. & ECKHARDT, B. 2016 Streamwise decay of localized states in channel flow. *Phys. Rev. E* **94** (4), 1–5.
- ZHU, K. & RICCO, P. 2024 Nonlinear evolution of vortical disturbances entrained in the entrance region of a circular pipe. *J. Fluid Mech.* **998**, A19.